The Tides of the Red Sea

David T. Pugh, Yasser Abualnaja and Ewa Jarosz

Abstract

This paper describes the present tidal regime in the Red Sea. Both the diurnal and the semidiurnal tidal amplitudes are small because of the constricted connection to the Gulf of Aden and the Indian Ocean, at the Bab el Mandeb Strait. Semidiurnal tides have a classic half-wave pattern, with a central amphidrome, zero tidal range, between Jeddah and Port Sudan. We present a high resolution numerical model output of several tidal constituents, and also model the amphidrome position in terms of ingoing and outgoing tidal Kelvin waves. We quantify the energy budgets for fluxes and dissipation.

Introduction

The Red Sea is a semi-enclosed, narrow basin that extends between latitudes 12.5^{o}N and 30°N, with an average width of 220 km, a mean depth of 524 m (Morcos 1970; Patzert 1974), and maximum recorded depths of about 3000 m. Toward the north, it ends in two narrow gulfs, the Gulf of Suez with an average depth of 40 m and the Gulf of Aqaba with depths over 1800 m (Fig. 2.1a, b). The only significant opening to the Indian Ocean is at its southern end through the shallow and narrow Bab el Mandeb Strait (a sill depth of 160 m and a minimum width of about 25 km) where it communicates with the Gulf of Aden.

D. T. Pugh (✉)
National Oceanography Centre, Joseph Proudman Building, 6 Brownlow Street, Liverpool, L3 5DA, UK
e-mail: d.pugh@me.com

Y. Abualnaja
Red Sea Science and Engineering Research Center, King Abdullah University of Science and Technology (KAUST), Thuwal, Saudi Arabia

E. Jarosz
Naval Research Laboratory, Oceanography Division Stennis Space Center, Stennis Space Center, MS 39529, USA

Seas that are connected with the open ocean through narrow straits are generally characterized by small tidal ranges (Defant 1961). Because of the restricting Bab el Mandeb Strait, the Red Sea tides are relatively small compared with those of the open ocean, and with those generally experienced along coasts near continental shelves. The semidiurnal oscillations predominate with maximum ranges on spring tides of about one metre in the far north at Suez, and in the southern entrance near Perim Island.

The length and depth of the Red Sea give near-resonant half-wavelength dynamics for the semidiurnal tide, which on a rotating Earth results in a wave progression around an amphidrome (a point with zero tidal amplitude) roughly located between Jeddah and Port Sudan, as shown in Fig. 2.2. The diurnal tides are only a few centimetres in range throughout the Red Sea, being most evident in the records from around Port Sudan, in comparison with the locally very small semidiurnal tidal ranges.

In the north, where the Red Sea divides into the Gulf of Aqaba and the Gulf of Suez, the two marginal gulfs have very different tidal regimes. The Gulf of Suez is shallow and interspersed with small islands. It has a mean depth of 36 m, and a natural period of 6.7 h; there is a semidiurnal amphidrome in the Gulf of Suez, and the strong currents imply an area of high local tidal energy dissipation.

The Gulf of Aqaba has a mean depth of 650 m and a natural oscillation period of about 0.9 h (Defant 1961). The Gulf of Aqaba tides oscillate in phase with the adjacent Red Sea with a 35 min lag from the entrance at the Strait of Tiran, to the head of the Gulf, typical of a standing wave (Monismith and Genin 2004). Tidal currents in the Gulf of Aqaba appear to be associated with internal wave generation; as tidal currents flow through the Strait of Tiran, they drive internal tidal waves on the internal density interface. Their strength varies considerably throughout the year, influenced by varying density stratification.

Despite the small tidal range, the semidiurnal tide of the Red Sea has been important in the development of general scientific ideas about the tides, as discussed by Defant

Fig. 2.1 **a** Map of the Red Sea, Bab el Mandeb Strait, Gulf of Aden and northwestern Indian Ocean, Dahlak and Farasan Banks, and the open ocean boundary of the model (dotted line); depth contours are in metres; **b** Locations of the sea level stations from heritage data subsurface pressure gauges (G89, G108, G109) all black circles. Those marked in red are sites of new observations for this study
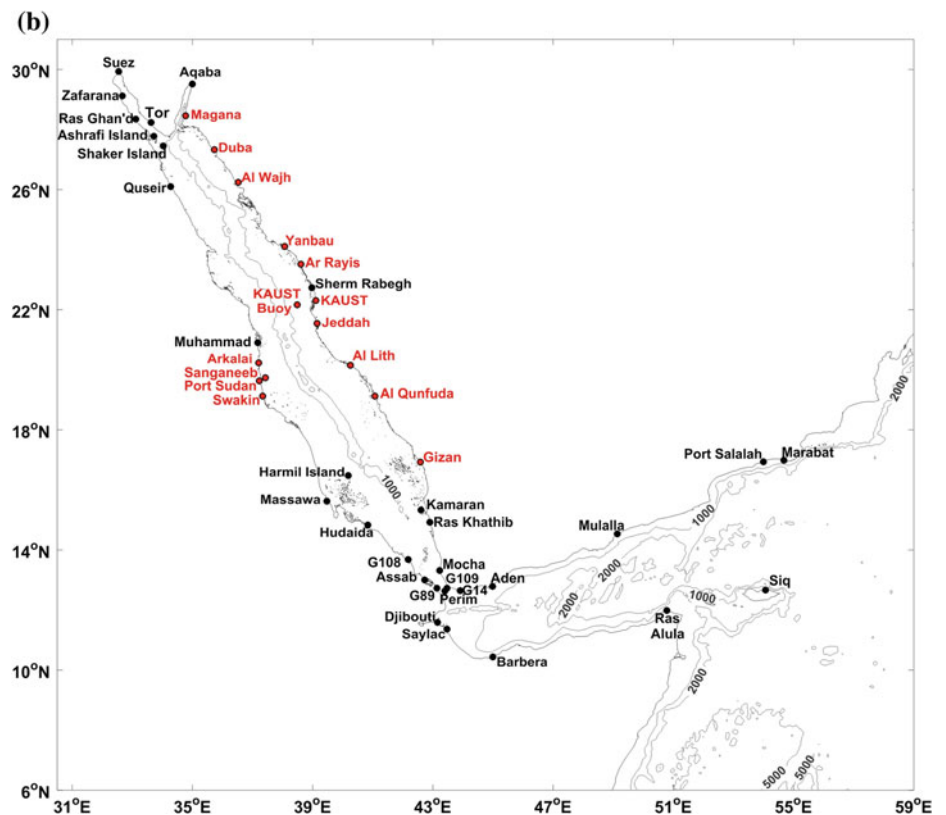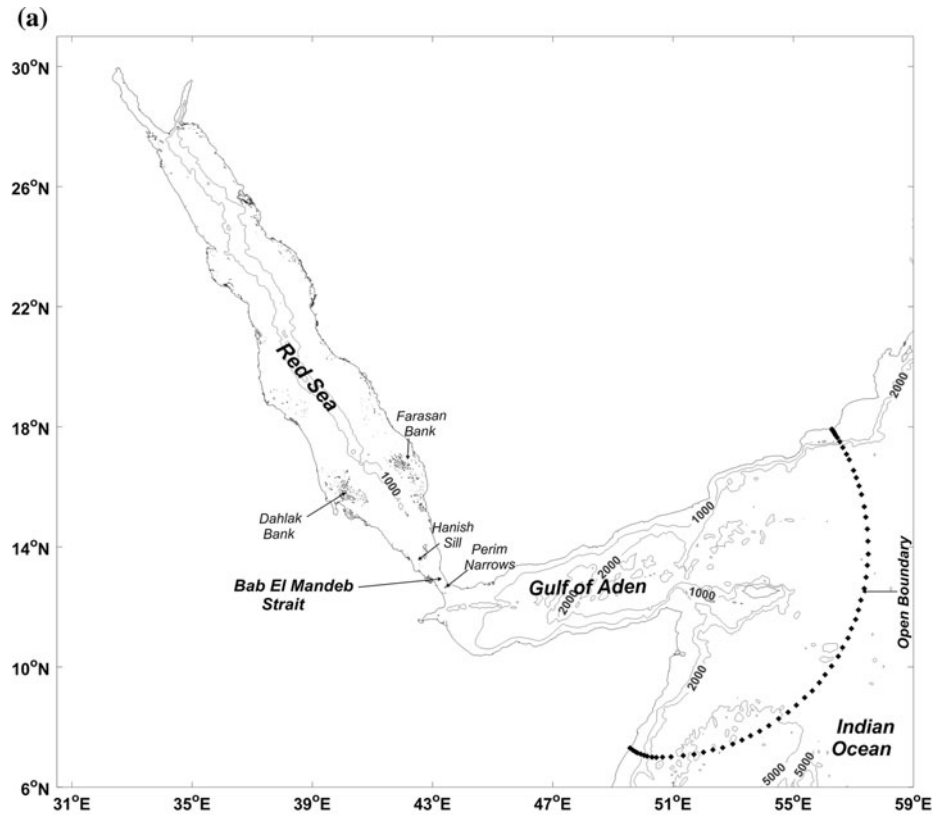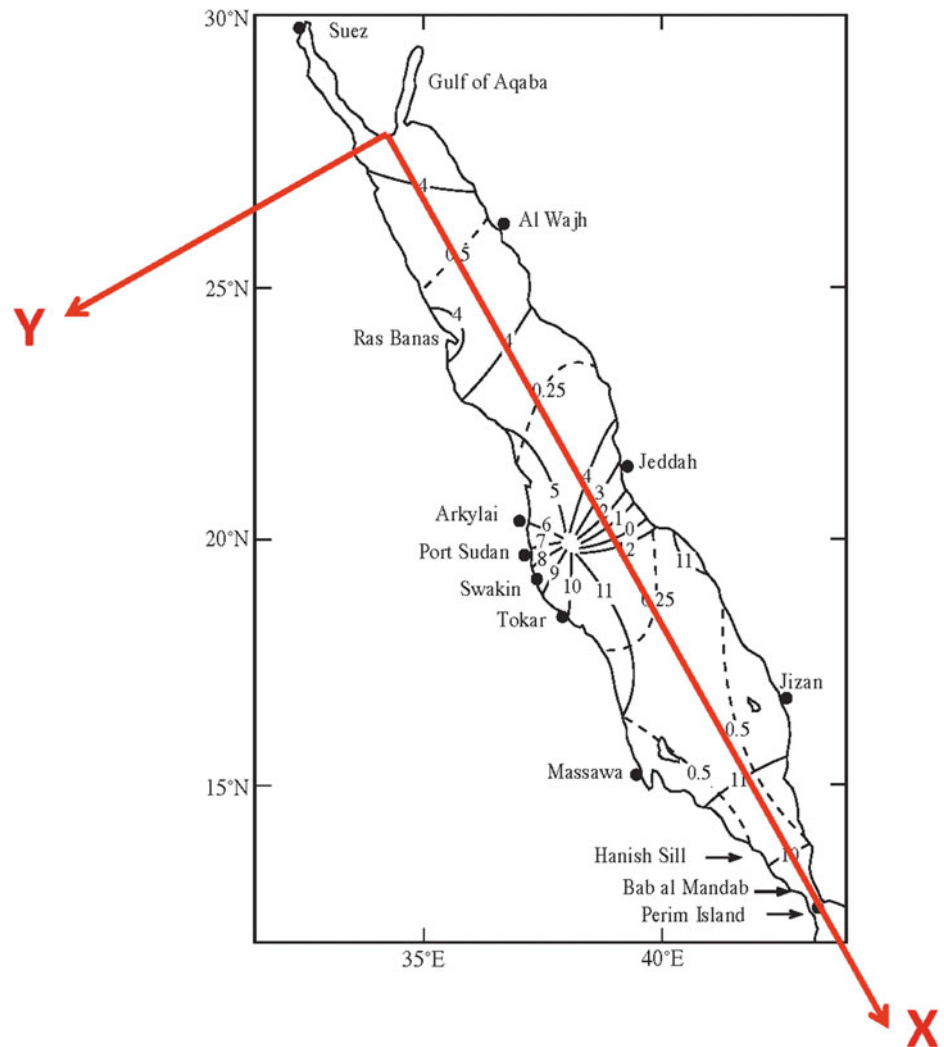
Fig. 2.2 Outline map of the semidiurnal lunar tidal range (M$_2$) in the Red Sea and locations of the recent measurements. The coordinate X–Y system is used for fitting Kelvin waves in Sect. 6 (DHI 1963)

(1961). Harris (1898) was the first to explain dynamically the tides in the Red Sea in terms of the superposition of a standing wave produced by the tide generating forces and a progressive wave entering through the Bab el Mandeb Strait. Because of its long narrow shape and deep sides, the Red Sea was used as an early application of numerical computations of tides, before modern computer power made tidal modelling routine (Grace 1930). Proudman (1953) by modeling the Red Sea as 39 transverse sections along the axis, derived the behaviour of Red Sea tides as seiches in a one-dimensional basin; he also studied the influence of direct gravitational forcing within the Sea, in both cases without Earth rotation. The relative importance of tidal forcing through the Bab el Mandeb Strait, compared with direct gravitational forcing within the Red Sea itself, remained unclear. Defant (1961) called these external and direct forcing the *co-oscillating* and *independent* tides respectively; he suggested they are equally important, but also recommended consideration of the frictional energy losses, for a fuller description of the tidal dynamics.

Further recent evidence to help understand the Red Sea tidal budgets and energy dissipation, comes from detailed surveys of levels and currents at the southern end of the Red Sea (Jarosz et al. 2005a, b; Jarosz and Blain 2010). These surveys show a complicated system of tides with an amphidrome for M$_2$ between the Perim narrows and the Hanish Sill. Tides to the south, in the Perim Narrows are similar to those in the Gulf of Aden. Amplitudes become very small near Assab and then increase northward to the co-oscillating amplitudes shown in Fig. 2.2. The numerical model simulation developed for Jarosz and Blain (2010), which included the full Red Sea, is the one used here, but whereas in that paper the emphasis was on the details of the southern Perim Narrows tides, here we look at the results from the model for the more extensive Red Sea, and compare them with a series of new high quality Red Sea tidal analyses which were not available at that time.

The very high resolution model of the Red Sea tides, with both external and direct gravitational forcing, is described in detail. The results are then used to investigate the detailed

location and movement of the central semidiurnal amphidrome; we interpret these movements in terms of a model of a standing wave consisting of two Kelvin waves, one travelling northward along the Saudi Arabian coast, and a reflected wave travelling south along the Egyptian and Sudanese coast. We also address the traditional tidal question for the Red Sea: The relative importance of direct gravitational tidal forcing, and the external forcing by tides at the Bab el Mandeb Strait (Defant 1961). A general overview of sea level variability in the Red Sea, including weather, climate and tectonic effects, was published in an earlier volume in this series (Pugh and Abualnaja 2015).

Data Collection

Before discussing the details of the recent data collection programme, it is appropriate to outline the prior state of knowledge, and of sea level data availability. In short, apart from information published by Vercelli (1925, 1927, 1931) and by Defant (1961), and the secondary port data published in nautical tide tables, until recently there has been very little robust sea level data available for analysis. In many cases, much of the published values in these tide table volumes are based on only a few days of observational data. The longest periods of data were from Port Sudan. Scientific sea level research with these data includes (Sultan et al. 1995; Sultan and Elghribi 2003), Elfatih (2010), and Mohamad (2012) (see Pugh and Abualnaja 2015) for a full listing). Satellite altimetry data has provided an alternative perspective.

Coastal in Situ Data

These earlier coastal data were systematically collected and tabulated as a preparation for the numerical model of Red Sea tides which we detail later (Jarosz and Blain 2010). This numerical model was developed at the United States Naval Research Laboratory, as part of a joint KAUST-Woods Hole Oceanographic Institution physical oceanography research programme. The results have not previously been published in open scientific literature.

In Table 2.1, the tidal harmonic constituents actually in the Red Sea, collected for the Red Sea modelling project entitled "Observation and Modeling—an Integrated Study of the Transport through the Strait of Bab el Mandab" (the BAM project) (see also Murray and Johns 1997) are listed. These consist of data at 22 water level stations, including three subsurface pressure gauges. The three subsurface pressure gauges were deployed for the BAM study. The model also uses data from other sites outside the Red Sea. Data and geographical locations of the water level stations were obtained from the listings of the International Hydrographic Organization (1979). It must be noted that all the observed tidal amplitudes and phases come from near-coastal areas, so there is no check directly of the tidal elevations in open waters, and that many values are based on only short periods of data. In addition, as explained above, at some water level stations only a few tidal constituents were available for the comparison; the common constituents for all stations were O_1, K_1, M_2, and S_2. These are the principal lunar diurnal term O_1, the luni-solar diurnal term K_1, the principal semidiurnal lunar tide M_2 and the principal semidiurnal solar tide S_2. The locations are plotted in Fig. 2.1b.

The model was also compared with tidal information for seven sites outside the Red Sea, in the Gulf of Aden, but inside the model boundary shown in Fig. 2.1. The full set of tidal data used for model comparison, together with fuller details of the process and maps of four additional modelled smaller tidal terms (Q_1, P_1, N_2 and K_2) is available in the original technical report (Jarosz and Blain 2010).

For the subsurface pressure measurements, G89, G108 and G109, additional caution is necessary when considering the S_2 tidal constituent term. This is because subsurface pressures include changes in atmospheric pressures; it is appropriate to give some background information here.

In addition to gravitational forcing, there is another type of tidal forcing related to the solar heating variations, generally called *radiational forcing*. Detailed harmonic tidal analyses of atmospheric pressures show a daily constituent of 24 h period S_1. In addition, there is an S_2 constituent. Generally, the S_1 constituent, representing diurnal air pressure changes, is a global tropical phenomenon, sometimes enhanced by the local diurnal land/sea winds; the radiational S_2 constituent is driven by the twelve-hour oscillation of air pressure in the tropics. These air pressure tidal variations are included in subsurface pressure measurements, and must be corrected for. They are also, of course, potentially drivers of the measured marine tides.

Figure 2.3 shows the variations of air pressure over 5 days at KAUST, with both diurnal and semidiurnal components.

By the usual inverted barometer arguments, the atmospheric S_2 low atmospheric pressures which occur globally at approximately 04:00 and 16:00 local time, are equivalent to a maximum sea level increase of 12.5 mm at the equator. In the Red Sea, the S_2 atmospheric tide has an amplitude in the range 0.9–1.1 mbar (9–11 mm), decreasing with increasing latitude. The phase increases from east to west from 210 to 240 degrees relative to Greenwich, giving maximum pressures between 10:00 and 11:00 local time, and another pressure maximum between 22:00 and 23:00 local time (Ray and Ponte 2003).

However, the problem in making this correction in a specific region is that we cannot know the extent of the local

Table 2.1 Summary of earlier Red Sea tidal information, used for calibrating the numerical model. Amplitudes (H) in centimetres, phases (G) in UT. The final two columns show the amplitude ratio for the two principal semidiurnal tides, 0.46 in the Equilibrium Tide forcing; and the phase differences which are also the *age of the tide,* the number of hours after new and full moon that the maximum (spring) tides occur. Consistency of these parameters within sets of analyses is an indication of robust processes

	Location	Latitude (N)	Longitude (E)	O1		K1		M2		S2		H (S2/M2)	G (S2-M2)
				H	G	H	G	H	G	H	G		
1	Perim	12.63	43.40	18.0	351	35.0	350	37.0	136	17.0	159		
2	G89	12.73	43.13	15.0	345	30.0	340	23.0	121	14.0	142	0.61	21
3	G109	12.73	43.47	15.0	345	30.0	340	29.0	125	16.0	144	0.55	19
4	Assab	13.00	42.73	8.5	344	18.0	335	6.9	259	4.0	170	0.58	−89
5	Mocha	13.32	43.23	6.1	352	7.0	335	8.0	244	4.5	188	0.56	−56
6	G108	13.68	42.18	2.0	335	6.0	321	24.0	286	5.0	299	0.21	13
7	Hudaida	14.83	40.83	1.0	92	1.0	340	30.0	305	6.0	351	0.20	46
8	Ras Khathib	14.92	42.90	1.0	82	4.0	69	26.0	294	7.0	332	0.27	38
9	Kamaran	15.33	42.60	1.0	140	2.0	34	33.0	300	9.0	334	0.27	34
10	Massawa	15.62	39.47	2.0	184	2.3	16	33.4	328	12.4	332	0.37	4
11	Harmil Island	16.48	40.18	1.0	180	2.0	166	13.0	318	3.0	334	0.23	16
12	Port Sudan	19.60	37.23	2.0	170	2.0	168	1.0	204	1.0	256	1.00	52
13	Muhammad	20.90	37.17	2.0	175	3.0	166	6.0	132	1.0	185	0.17	53
14	Jeddah	21.52	39.13	1.0	161	2.8	156	6.0	109	1.0	132	0.17	23
15	Rabegh	22.73	38.97	4.0	162	4.0	156	11.0	124	2.0	165	0.18	41
16	Quseir	26.10	34.27	2.0	192	2.0	158	22.0	112	5.0	139	0.23	27
17	Shaker Island	27.45	24.03	1.0	178	2.0	167	25.0	117	4.0	144	0.16	27
18	Ashrafi Islands	27.78	33.72	1.0	153	2.0	167	25.0	118	4.0	145	0.16	27
19	Tor	28.23	33.62	2.0	159	4.0	164	8.0	205	1.0	230	0.13	25
20	Ras Ghan'd	28.35	33.12	2.0	157	2.0	160	18.0	274	7.0	302	0.39	28
21	Zafarana	29.12	32.67	1.0	199	3.0	165	42.0	280	12.7	301	0.30	21
22	Aqaba	29.52	35.00	1.0	146	2.0	158	28.0	128	8.0	155	0.29	27
23	Suez	29.93	32.55	1.3	170	4.5	158	56.0	278	14.0	306	0.25	28
				4.0		7.4		22.2		6.9		0.33	19.3

Fig. 2.3 Air pressures from the KAUST offshore buoy showing regular daily cycles
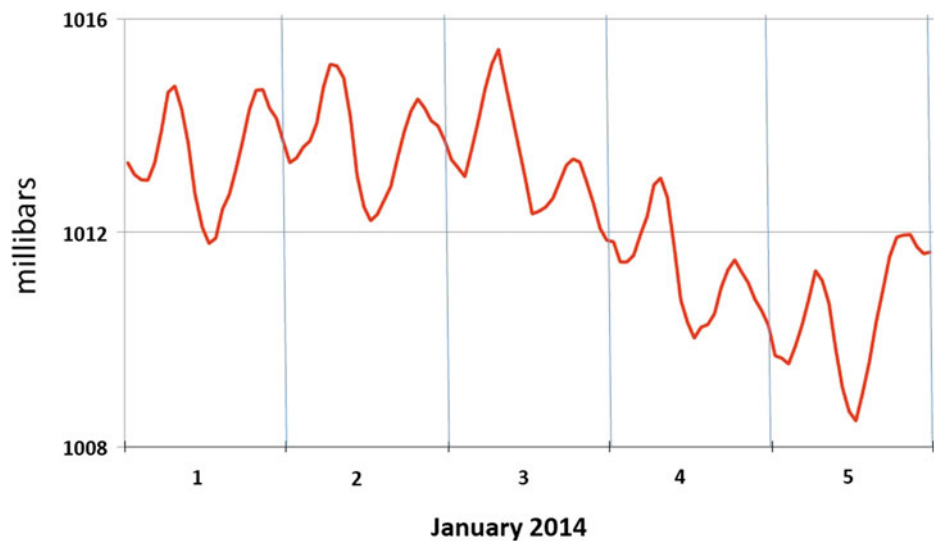
inverse barometer effect on sea levels. If the sea levels make a full and immediate inverted barometer response, then the subsurface pressures will be a measure of the gravitational tide. But if there is only partial compensation for the air pressure forcing the measured subsurface pressures will be both gravitational and partly radiational. For these reasons caution is necessary in analyses and hydrodynamic interpretation of the S_2 tide and to a lesser extent the K_1 tide, especially where the gravitational tides are small, for example near amphidromes.

To improve the availability of tidal constituents in the Red Sea, we have benefited from the recent long-period measurements, as given in Table 2.2. These fall into four groups:

- Subsea *pressure measurements* at four sites in Sudan, concentrated around the semidiurnal amphidrome; these were made with assistance from Elfatih Bakry Ahmed Eltaib, researcher in physical oceanography at the Institute of Marine Research, Red Sea University, Port Sudan;

- Three *subsurface pressure* measurements in Saudi Arabia, also near the amphidrome, as part of the KAUST Red Sea observing programme;
- Sea *level* data from seven sites, established since 2012 as part of the Saudi General Commission for Survey new sea level network. The seven General Commission for Survey permanent gauges along the whole length of the Saudi Arabia coast are high quality Aquatrak acoustic measurements of water levels;
- Current and air pressure measurements at the KAUST buoy mooring (Fig. 2.1b); the current components convention is: X positive along the Red Sea to the north, and Y positive across the Red Sea to the east.

The values of tidal amplitudes and phases for the major terms are summarised in Table 2.3. The final two columns in Table 2.3 show the ratio of the S_2/M_2 amplitudes, and the S_2 minus M_2 phase differences in the tidal constituents. These values are a useful check on the consistency of the analyses among themselves, in the region. The one exception to the

Table 2.2 Locations of new sea level measurements and sources. Red Sea University IMR is located in Port Sudan; GCS is the Saudi General Commission for Survey. Gauge manufacturers are accessible on the Web

Location	Latitude (N)	Longitude (E)	Gauge	Parameter	Measuring authority	Months	Period
Swakin	19.12	37.34	RBR 420-TG	SSP	Red Sea University IMR	7.5	25 Feb 2013 to 7 Sept 2013
Port Sudan	19.63	37.22	RBR 420-TG	SSP	Red Sea University IMR	7.5	25 Feb 2013 to 7 Sept 2013
Sanganeeb	19.73	37.43	RBR 420-TG	SSP	Red Sea University IMR	6	14 May 2015 to 18 Oct 2015
Arkalai	20.23	37.20	RBR 420-TG	SSP	Red Sea University IMR	7.5	25 Feb 2013 to 7 Sept 2013
Al Lith	20.15	40.26	SBE Seagauge	SSP	KAUST	12	26 June 2013 to 15 June 2014
KAUST	22.31	39.11	RBR 420-TG	SSP	KAUST	6	6 Mar 2013 to 7 Sept 2013
Ar Rayis	23.52	38.61	SBE Seagauge	SSP	KAUST	12	5 June 2014 to 28 May 2015
Gizan	16.93	42.58	Aquatrak 5000	Level	GCS	12	1 April 2014 to 31 March 2015
Al Qunfuda	19.12	41.07	Aquatrak 5000	Level	GCS	12	1 April 2014 to 31 March 2015
Jeddah	21.54	39.15	Aquatrak 5000	Level	GCS	12	1 April 2014 to 31 March 2015
Yanbau	24.11	38.07	Aquatrak 5000	Level	GCS	12	1 April 2014 to 31 March 2015
Al Wajh	26.24	36.52	Aquatrak 5000	Level	GCS	12	1 April 2014 to 31 March 2015
Duba	27.33	35.73	Aquatrak 5000	Level	GCS	12	1 April 2014 to 31 March 2015
Magana	28.46	34.77	Aquatrak 5000	Level	GCS	12	1 April 2014 to 31 March 2015

Table 2.3 Principal tidal constituents from the new measurements listed in Table 2.2. See Table 2.1 for details of the final two columns. Note the increased consistency among the analyses for this new data. Data from the KAUST buoy are for air pressures and current measurements (see text)

Location	Latitude (N)	Longitude (E)		O1		K1		M2		S2		H(S2/M2)	G(S2-M2)
				H	G	H	G	H	G	H	G		
Swakin	19.12	37.34		2.1	159	3.4	168	1.0	176	1.3	245	1.30	69
Port Sudan	19.63	37.22		2.0	159	3.2	166	1.7	142	1.3	230	0.76	88
Sanganeeb	19.73	37.43		1.6	144	2.5	163	1.7	140	1.3	230	0.76	91
Arkalai	20.23	37.20		1.8	160	3.1	170	2.7	131	1.3	214	0.48	83
Al Lith	20.15	40.26		1.8	159	2.8	159	2.5	329	0.9	277	0.36	−52
KAUST	22.31	39.11		1.6	166	2.8	222	11.0	115	3.2	158	0.29	43
Ar Rayis	23.52	38.61		1.5	169	2.8	164	14.6	115	4.5	153	0.31	38
Gizan	16.93	42.58		1.7	136	2.1	132	32.0	295	10.4	326	0.33	31
Al Qunfuda	19.12	41.07		1.7	131	2.6	148	8.3	294	3.2	326	0.39	32
Jeddah	21.54	39.15		1.7	154	3.4	155	7.1	97	1.6	122	0.23	25
Yanbau	24.11	38.07		1.4	158	2.8	156	16.4	101	4.5	124	0.27	23
Al Wajh	26.24	36.52		1.1	159	3.4	146	23.3	103	6.9	124	0.30	21
Duba	27.33	35.73		1.1	161	2.6	157	24.9	103	7.1	125	0.29	22
Magana	28.46	34.77		1.0	169	2.4	152	27.5	110	8.0	135	0.29	25
KAUST Buoy	22.30	38.09											
			Air pressure (mb)	0.05	91	0.47	61	0.07	21	1.05	194		
			X currents (cm/s)	0.49	213	0.62	340	0.79	31	0.32	96		
			Y currents (cm/s)	0.67	135	0.88	217	1.87	59	0.92	52		
			deg/hour	**speed**		**13.94**		**15.04**		**28.98**		**30**	

general internally consistent pattern, is the phase difference et al. Lith, which is minus 52^0. Elsewhere the differences are always positive and locally consistent. This difference is a measure of the *age of the tide*, the time between new or full moon and maximum semidiurnal spring tidal ranges (see Pugh and Woodworth 2014, p. 76). For all the sea level measurements made by the Saudi General Commission for Survey, the age of the tide is from 21 to 32 h; for the sub-surface pressure measurements around Port Sudan the age is consistently around 70–90 h. This is probably due to the effects of the separate M_2 and S_2 amphidromes differing slightly as the M_2 tidal wavelength is slightly longer (lower frequency). Similarly, the negative age et al. Lith can occur near an amphidrome. Also, the ages of the tides as measured on the pressure instruments may be affected by the air pressure and because of inexact adjustments for the S_2 inverted barometer response discussed above.

For tides near the central semidiurnal amphidrome where the tidal signal is small and comparable with meteorological "noise", it is reasonable to ask whether repeated analyses can produce stable tidal constituents. Table 2.4 shows the results for four long-term KAUST measurements et al. Lith. The periods analysed are either a year, or in the first case six-months. For example, M_2 has amplitudes which range

between 2.4 and 2.5 cm, with phases between 327^0 and 331^0, a span equivalent to only eight minutes. This agreement from year to year is remarkably good even down to the one-millimetre level, and even applies to some very small gravitational terms such as the thrice-daily M_3 term. This clearly shows that the actual observed tides are very stable at a fixed location even very close to the amphidrome.

Altimetry Data

The various long-term satellite altimetry missions have allowed tidal mapping from space using altimeter measurements of sea levels, generally with an accuracy of about 0.02 m. The sampling intervals, both in time and space call for very different analysis techniques from the traditional processing of regular measurements at fixed coastal sites. Figure 2.4 shows the co-tidal chart for the M_2 tidal constituent for the Red Sea based on Topex/Poseidon measurements and inverse dynamic modelling techniques developed by Egbert and Erofeeva (2002). By solving in frequency space, otherwise considerable computational effort is much reduced. The web site for the Oregon State University offers tools for generating tidal maps for several

Table 2.4 Al Lith tidal constituents, showing the remarkable stability of the principal tidal constituents, from four different long periods of sub-surface pressure measurements, even at the millimetre level

Constituent	Speed			Amplitude (cm)						Phases (degrees)					
	Deg/h		2011	2012	2013–14	2014–15	Mean	Range	2011	2012	2013–14	2014–15	Mean	Range
O1	13.943		1.723	1.791	1.723	1.791	1.757	0.1	160	161	158	157	159	4
K1	15.0411		2.274	2.756	2.756	2.825	2.653	0.7	155	159	160	160	159	5
N2	28.4397		0.965	0.896	0.896	0.896	0.913	0.1	332	329	326	328	329	6
M2	28.9841		2.412	2.412	2.549	2.480	2.463	0.2	331	327	329	329	329	4
S2	30		0.896	0.896	0.965	0.896	0.913	0.1	278	277	276	277	277	3
K2	30.0821		0.276	0.345	0.276	0.276	0.293	0.1	317	326	320	320	321	9
M3	43.4761		0.345	0.276	0.276	0.207	0.276	0.1	283	282	301	312	295	29
Standard Dev (m) before analysis	0.15	0.18	0.20	0.20	**Data Blocks**	2011 May to November 2012								
Standard Dev (m) after analysis	0.08	0.09	0.10	0.11		2012 is November 2011 to December 2012								
Tidal variance %	33	25	24	27		2014 is June 2014 to May 2015								
Non-tidal variance %	67	75	76	73										

regions including the Red Sea, where the resolution is $1/60^0$. The Oregon State University package, called OTIS (OregonSU Tidal Inversion Software) captures ninety percent of the Red Sea sea-level variability in this map of the M_2 constituent (http://volkov.oce.orst.edu/tides/region.html). Agreement with the coastal observations is good, with all the general features reproduced. Local coastal differences from the general patterns, for example et al. Wajh, are not always captured.

Currents

The only available systematic measurements of currents are from the KAUST buoy system. The KAUST buoy is a long-term installation measuring currents with an acoustic current meter at several depths, air pressures, but not bottom pressures. The location is 22.30^0N, 38.09^0E, some 50 km off the Saudi coast, which at this latitude trends mainly south to north, rather than the overall Red Sea alignment of 23.5 degrees west of north. The water depth at the site is around 700 m.

The currents at the KAUST buoy were measured by an acoustic Doppler current meter, in 4 m depth levels. We averaged currents in the bands from 15 to 91 m depths, and resolved them into north and east components. Data were from 7 December 2014 to 28 February 2015. There was considerable vertical current shear and variability, but the averaged values as summarised in Table 2.5 were consistent. Note that the tidal currents are only about 10% of the observed current variance, or kinetic energy at this site.

Theoretical Background

Standing Waves

The two key factors in understanding the Red Sea tides are:

- Due to the length and depth of the Red Sea, a natural period of seiche is very close to that for half a semidiurnal tidal wavelength, and a quarter of a diurnal wavelength.
- The tidal amplitudes are small because of attenuation of external Indian Ocean forcing by the narrow Bab el Mandeb Strait in the south.

The resonant effect is explained as follows. For gravity oscillations of water in an enclosed basin the natural period is given by Merian's Formula:
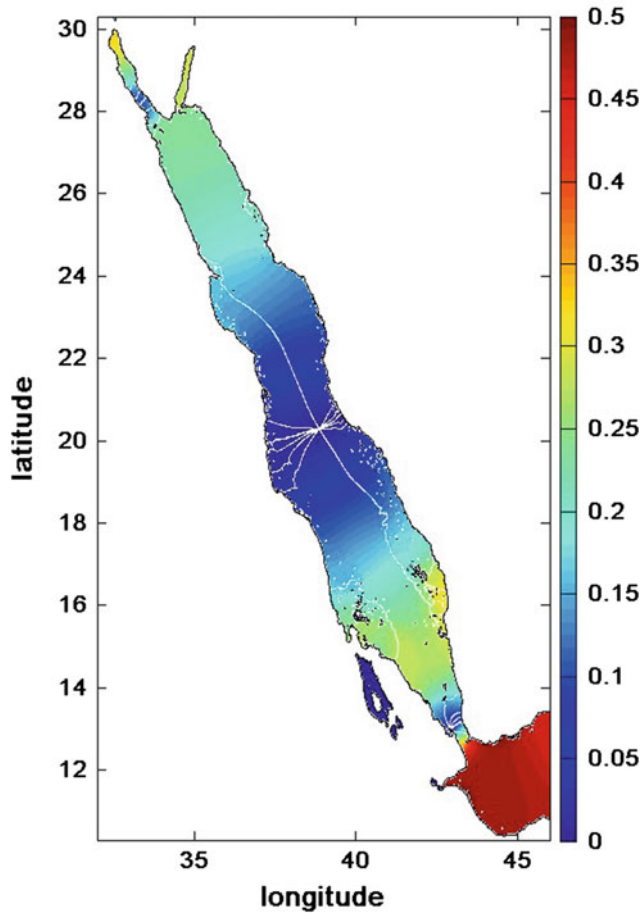
Fig. 2.4 Co-tidal M_2 chart of the Red Sea based on altimetry data (Egbert and Erofeeva 2002). The lines running northwest and southeast along the Red Sea axis are 5 h and 11 h phase lag on UT, respectively

$$Natural\,period = \frac{2 \times sea\,length}{\sqrt{g \times water\,depth}} = \frac{2L}{\sqrt{gD}} \quad (1)$$

For the Red Sea length of about 1600 km and a representative depth of 500 m the natural period is 12.6 h, close to semidiurnal resonance.

A Two-Wave Model

We can model the central Red Sea semidiurnal tide as two oppositely travelling Kelvin waves, because of the standing wave system. A brief theoretical description follows.

The forces that describe the motion of ocean currents in a rotating-Earth system cause a deflection of the currents toward the right of the direction of motion in the northern hemisphere and conversely in the southern hemisphere. The wave motion on this rotating system can be written as a Kelvin wave (Taylor 1920, 1922; Pugh and Woodworth 2014):

$$H(x, y, t) = H_0 \exp\left(\frac{-fy}{c}\right) \cos\left(\omega t - \frac{x}{c}\right) \quad (2)$$

using a coordinate system as shown in Fig. 2.2. H is the water level, c is the wave speed $\sqrt{gD}$, and f is the Coriolis parameter. ω is the wave angular speed, t is the time variable and H_0 is the amplitude at $y = 0$.

Kelvin waves have the characteristic that rotation influences the way in which the wave amplitude decreases across the channel away from the value H_0 at the y = 0 boundary as shown in Fig. 2.5a (in the northern hemisphere). The wave heights and currents have amplitudes:

$$H(y) = H_0 \exp\left(\frac{-fy}{c}\right)$$
$$U(y) = \left(\frac{g}{D}\right)^{\frac{1}{2}} H(y) \quad (3)$$

Table 2.5 Comparison of observed and modelled currents at the KAUST buoy. Here X and Y directions are geographic east and north, not as in Fig. 2.2 and later amphidrome analyses

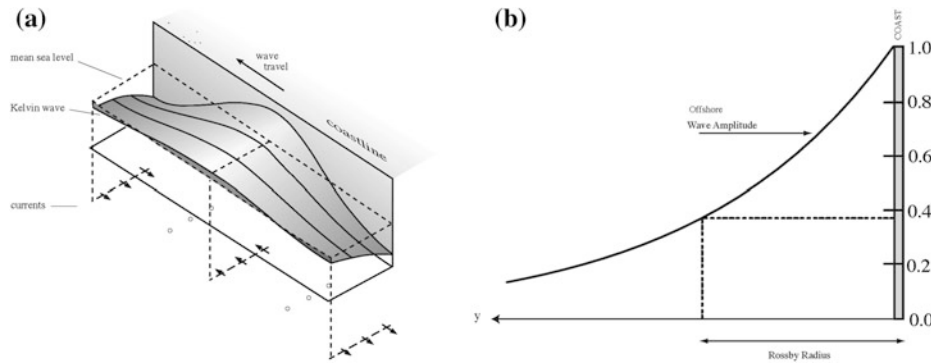| Observations														
		O1		K1		M2		S2	Tidal	Residual			Major axis	
	H	G	H	G	H	G	H	G	Variance	Current			Alignment	For M2
X (east)	0.49	213	0.66	340	0.79	31	0.32	96	20%	−12	cm/sec		17 degrees	East of north
Y (north)	0.67	135	0.88	217	1.88	59	0.92	52	8%	−8	cm/sec			
Model														
X (east)	0.005	299	0.01	290	0.06	239	0.03	265					3 degrees	East of north
Y (north)	0.15	67	0.33	66	1.34	36	0.57	64						

Fig. 2.5 K wave dynamics (after Pugh and Woodworth 2014): **a** A three-dimensional illustration of the elevations and currents for a Kelvin wave running parallel to a coast on its right-hand side (northern hemisphere). The normal dynamics of wave propagation are altered by the effects of the Earth's rotation which act at right angles to the direction of wave travel; **b** A two-dimensional section across the Kelvin wave at high tide, showing how the tidal amplitude falls away exponentially from the coast; at one Rossby radius the amplitude falls to 0.37 of the coastal amplitude. The wave is travelling into the paper

The exponential amplitude decay law has a scale length of c/f, which is called the barotropic Rossby radius of deformation. At a distance $y = c/f$ from y = 0 the amplitude has fallen to 0.37 H_0. The wave speed is the same as for a non-rotating case, and the currents are always parallel to the direction of wave propagation. Figure 2.5b shows the profile across a Kelvin wave. Note that Kelvin waves can only move along a coast in one direction; this is with the coast on the right in the northern hemisphere.

Figure 2.6 shows the co-tidal (equal phase) and co-amplitude (equal amplitudes and ranges) lines for a Kelvin wave reflected without energy loss at the head of a rectangular channel (Taylor 1922). The sense of rotation of the wave around the amphidrome is anticlockwise in the northern hemisphere and clockwise in the southern hemisphere. The co-tidal lines all radiate outward from the amphidrome and the co-amplitude lines form a set of nearly concentric circles with the centre at the amphidrome at which the amplitude is zero. The amplitude is greatest around the boundary of the basin. Figure 2.7 shows this displacement increasing as the reflected Kelvin wave is made weaker (Pugh 1981).

For a reflected Kelvin wave, the first amphidrome, where the incident and reflected waves cancel, is located at a position:

$$x = \frac{\pi c}{2\omega} \qquad (4a)$$

$$y = \frac{-c \ln \alpha}{2f} \qquad (4b)$$

Here α is the amplitude ratio of the reflected wave to the incident wave. In the Red Sea, the semidiurnal tides are approximately a standing wave in an almost enclosed narrow basin on the rotating Earth. A standing tidal wave is represented by two Kelvin waves, travelling in opposite directions. The tidal progression rotates about the nodal point, which is a central tidal amphidrome.

The incoming wave travels northward with a maximum amplitude along the coast of Saudi Arabia. At the northern end, the shallow water of the Gulf of Suez is a locally important area of energy loss due to the strong tidal currents, and bottom friction. Because of the energy loss, the tidal wave is not perfectly reflected. The reflected southward, slightly weaker, wave has a maximum amplitude along the coast of Egypt, Sudan and Eritrea.

Because the reflected Kelvin wave is weaker than the incident Kelvin wave, the amphidrome is displaced from the centre of the channel to the left of the direction of the incident wave; hence the central semidiurnal amphidrome is displaced toward the Sudan coast.

In a narrow channel, an amphidromic point may move outside the left-hand boundary, and in this case, although the full amphidromic system shown in Fig. 2.6 is not present, the co-tidal lines will still focus on an inland point. This is called a virtual or degenerate amphidrome. The tides of the Gulf of Suez have this degenerate amphidrome characteristic.

The expressions in Eq. 4a for the amphidrome location in x and y have the advantage in separating the effects of the two physically variable quantities, the angular speed ω, and the amplitude attenuation coefficient of the reflected wave, α. The effects of each on the amphidromic position and movement are orthogonal to each other and so may be considered independently in the section below on locating the amphidrome.

Fig. 2.6 Amphidrome dynamics: A three-dimensional drawing exaggerated to illustrate how a tidal wave progresses around an amphidrome in a basin in the Northern Hemisphere. The red numbers are hours in the semidiurnal cycle (after Pugh and Woodworth 2014)
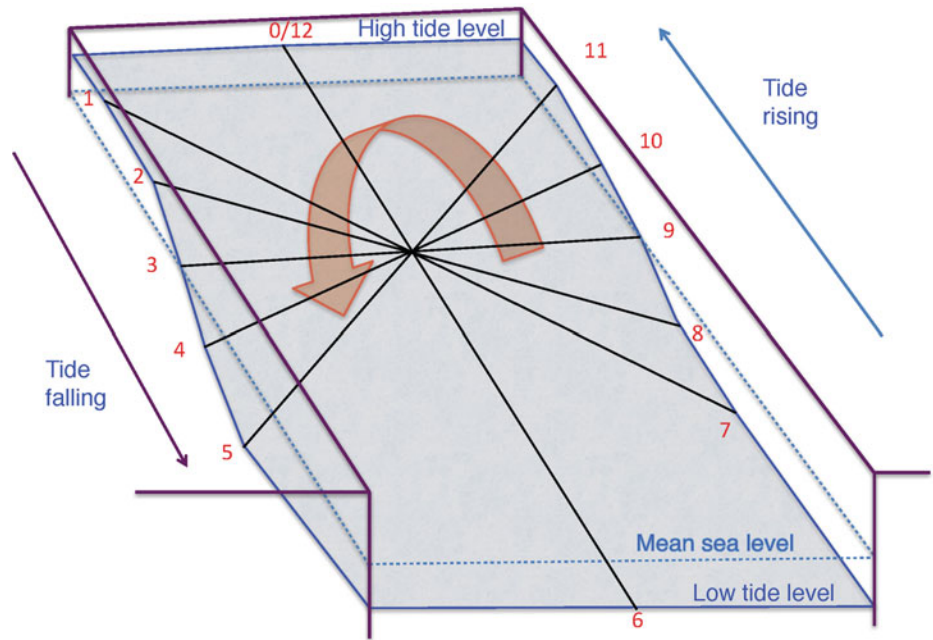
Consider first the effect of changing angular speed ω on the x position. Although for a single tidal constituent the frequency and period are fixed, on a daily basis the frequency of the semidiurnal tides is slightly modulated, notably through a spring-neap 14 day cycle. This is because the speeds of M_2 and S_2, being 28.98^0/h and 30^0/h respectively, when combined have frequencies that vary in the range:

$$\frac{H_{M_2}\omega_{M_2} + H_{S_2}\omega_{S_2}}{H_{M_2} + H_{S_2}} \quad \text{and} \quad \frac{H_{M_2}\omega_{M_2} + H_{S_2}\omega_{S_2}}{H_{M_2} + H_{S_2}} \quad (5)$$

As we show in the section on locating the amphidrome, this range is from 29.29^0/h to 28.18^0/h for the Red Sea M_2 and S_2 amplitudes (Lamb 1932).
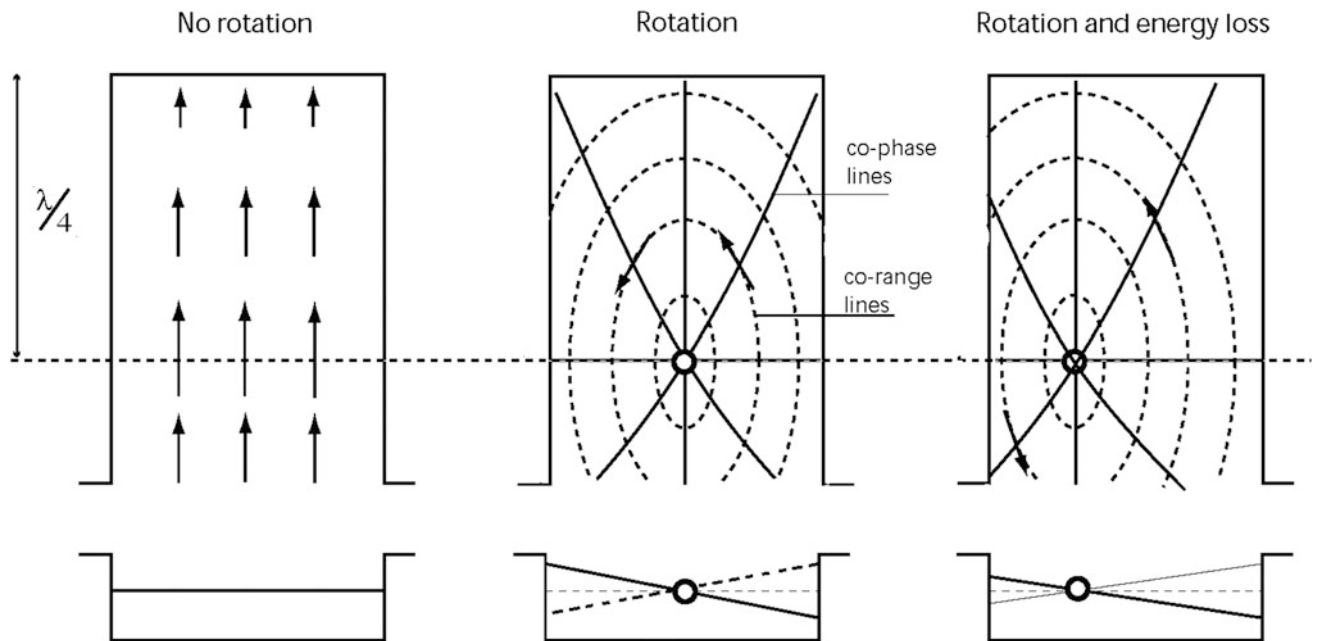
Fig. 2.7 Amphidrome dynamics: The effects of the Earth's rotation on a standing wave in a basin which is slightly longer than a quarter-wave length. With no rotation, there is a line of zero tidal amplitude. Because of the Earth's rotation, the tidal wave rotates around a point of zero amplitude, called an amphidromic point. In the third case, because the reflected wave has lost energy through tidal friction, the amphidrome is displaced from the centre line. (after Pugh and Woodworth (2014)

Numerical Modelling

Modelling Details

Yang et al. (2013) developed a two-dimensional finite element model of tides in the Red Sea and the Gulf of Aden. Their model boundary is in the Indian Ocean at 56^0E; at this boundary, the model is driven by predicted tides based on five constituents, O_1, P_1, K_1, M_2 and S_2. There are 21836 triangular area sectors. The outputs from their model include co-tidal charts for the Gulf of Aden, and some small plots of O_1, K_1, M_2 and S_2 tides in the Red Sea, but there is little detail available.

Abohadima and Rakha (2013) developed a depth-integrated finite element model for the Red Sea to predict the tidal currents and tidal water level variations. The open boundary for their model is located at the Bab el Mandeb Strait, and the driver is the predicted levels at the Strait. The model had an element size varying from 15 km to less than 1 km. The output is only in terms of time variations of tidal levels and no attempt is made to look at individual tidal constituents in the elevations. The maximum tidal currents at springs are mapped, and show speeds of up to 20 cm/s. There is no direct gravitational forcing.

Madah et al. (2015) present a numerical model study of the Red Sea tides, with external forcing in the Gulf of Aden, 63434 grid cells, and 5 km grid spacing. They also reproduce the general tidal features, but check these against only limited observational data.

The numerical model results presented in this chapter are from Jarosz and Blain (2010), where fuller details are available. The model domain, shown in Fig. 2.1a, includes the Red Sea, Bab el Mandeb Strait, Gulf of Aden and the northwestern part of the Indian Ocean. The model area was chosen primarily to reproduce tidal waves propagating from the Indian Ocean, which is a significant forcing of tidal motion in the Red Sea as discussed by Defant (1961); having a more remote external model boundary avoids having a boundary in the locality of the complicated Bab el Mandeb Strait tidal dynamics. Depth information for the model was obtained from two sources: The Naval Oceanographic Office Digital Bathymetric Data Base-Variable Resolution (DBDB-V) (NAVOCEANO 1997) and charts published by the Defense Mapping Agency in 2006.

The finite element grid used in these computations is displayed in Fig. 2.8. It consists of 84,717 nodes and 163,854 elements. Nodal spacing for this mesh varies throughout the modelled region and ranges between 0.2 and 56 km with the highest refinement present in the Bab el Mandeb Strait and the Red Sea where the minimum and maximum nodal spacings are 0.2 and 5.5 km, respectively. The coarsest resolution is located in deep waters of the Gulf of Aden and Indian Ocean.

The two-dimensional form of the model is based on vertically integrated equations of motion and continuity, which, in a spherical coordinate system, are defined as follows (Gill 1982):

$$\frac{\partial U}{\partial t} + \frac{U}{R\cos\varphi}\frac{\partial U}{\partial \lambda} + \frac{V}{R}\frac{\partial U}{\partial \varphi} - fV - \frac{UV\sin\varphi}{R\cos\varphi}$$
$$= -\frac{g}{R\cos\varphi}\frac{\partial}{\partial \lambda}(\zeta - \alpha\eta) - \frac{\tau_{b\lambda}}{\rho_0 H} \quad (6a)$$

$$\frac{\partial V}{\partial t} + \frac{U}{R\cos\varphi}\frac{\partial V}{\partial \lambda} + \frac{V}{R}\frac{\partial V}{\partial \varphi} + fU + \frac{UV\sin\varphi}{R\cos\varphi}$$
$$= -\frac{g}{R}\frac{\partial}{\partial \varphi}(\zeta - \alpha\eta) - \frac{\tau_{b\varphi}}{\rho_0 H} \quad (6b)$$

$$\frac{\partial \zeta}{\partial t} + \frac{1}{R\cos\varphi}\frac{\partial(UH)}{\partial \lambda} + \frac{1}{R\cos\varphi}\frac{\partial(VH\cos\varphi)}{\partial \varphi} = 0 \quad (6c)$$

where t represents time, λ, φ denote degrees of longitude and latitude, R is Earth radius, ζ is the free surface elevation, U and V are the depth-averaged horizontal east-and north-directed velocities, respectively, $H = \zeta + h$ is the total water column depth, h is the bathymetric depth relative to the geoid, $f = 2\Omega\sin\varphi$ is the Coriolis parameter, Ω is the angular speed of the Earth, ρ_o is a reference density, g is the acceleration due to gravity, α is the Earth elasticity Love Number factor approximated as 0.69 for all tidal constituents as used by other investigators including Schwiderski (1980) and Hendershott (1981) (the slight frequency dependency (Wahr 1981) is not important here), η is the Newtonian Equilibrium tidal potential, and $\tau_{b\lambda}$, $\tau_{b\varphi}$ are the bottom stresses taken as:

$$\tau_{b\lambda} = \rho_0 C_d U\sqrt{U^2 + V^2}; \quad \tau_{b\varphi} = \rho_0 C_d V\sqrt{U^2 + V^2} \quad (7)$$

where C_d denotes the bottom drag coefficient.

The Equilibrium tidal potential is expressed as (Reid 1990):

$$\eta(\lambda, \varphi, t) = \sum_{n,j} C_{jn} f_{jn}(t_0) L_j(\varphi) \cos\left[2\pi(t - t_0)/T_{jn} + j\lambda + \upsilon_{jn}(t_0)\right]$$
$$(8)$$

where t is time relative to t_o, which is the reference time, C_{jn} is a constant characterizing the amplitude of tidal constituent n of species j, f_{jn} is the time-dependent nodal factor, υ_{jn} is the time-dependent astronomical argument, j = 0, 1, 2 are the tidal species (j = 0 declinational; j = 1 diurnal, j = 2 semidiurnal), $L_o = 3\sin^2\varphi - 1$, $L_1 = \sin(2\varphi)$, $L_2 = \cos^2\varphi$,
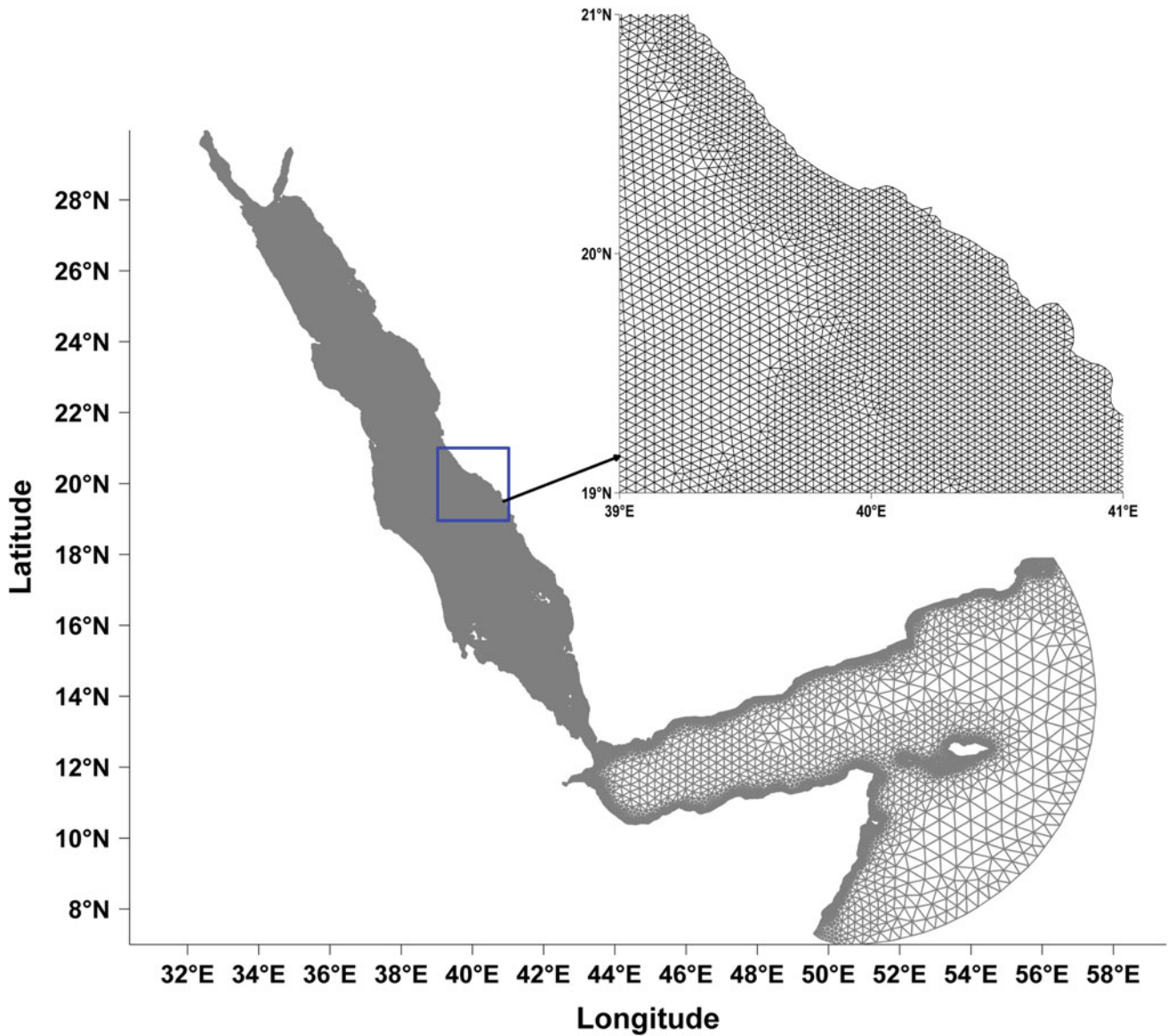
Fig. 2.8 Model finite element grid (84717 nodes and 163,854 elements) and an example of the model grid resolution within the central amphidrome area

and T_{jn} is the period of constituent n for species j. See Pugh and Woodworth (2014, Chap. 3) for a development of this expression involving tidal species, and for time dependence.

Although direct gravitational tidal forcing is in the model, with elastic-earth corrections, the secondary effects of elastic earth tidal loading, and gravitational self-attraction are not included in the equations.

Prior to being discretised, the continuity and momentum equations are combined into a Generalized Wave Continuity Equation (GWCE), which has been shown to have superior numerical properties to a primitive continuity equation when a finite element method is used in space (Lynch and Gray 1979). The final forms of the GWCE and momentum equations, which are solved by the model, are given in Blain

and Rogers (1998), while numerical discretization of these equations is described in detail by Luettich et al. (1992) and Kolar et al. (1994).

Additional model constraints at the land boundaries are:

- no flow across.
- friction-free tangential slip.

At the open ocean boundary, the tidal elevation is generated by synthesising four diurnal (K_1, O_1, P_1, Q_1) and four semidiurnal (M_2, S_2, N_2, K_2) constituents. The tidal harmonic constants used to generate the elevation along the open boundary are linearly interpolated onto the boundary nodes using data from the World Ocean Tide Model

database FES99 (Lefevre et al. 2002). In addition, an equilibrium tidal potential forcing within the domain is applied for the same eight constituents.

A time step of 15 s was used to ensure model stability based on the Courant number criterion. The parameter τ_o, which weights the primitive and GWCE form of the continuity equation, was estimated from a formula given by Westerink et al. (1994) and set equal to 0.001. Finally, the minimum depth was assigned to be 3 m to eliminate any potential drying of computational nodes since the wetting and drying option was not included in these simulations. The model simulations were carried out for one year to generate a sufficiently long time series that allows the separation of the P_1 constituent from the K_1 constituent; resolution of the S_2 constituent from the K_2 constituent was also possible. Boundary conditions are already adjusted for nodal effects. The amplitudes and phases of the tidal constituents were obtained through harmonic analysis programmes (Foreman 1977, 1978). Note that the analyses of the actual observations in Tables 2.3 and 2.4 were done using the UK National Oceanography Centre TASK software, but the two processes are entirely compatible for the constituents discussed here. However, for full analyses and comparisons there are significant differences, for example in defining the phases of the annual S_a constituent.

Several different model setups were utilized to simulate tides as close to those observed in the Red Sea as possible. The best fit to the observations was obtained when the model was driven only by external forcing, that is, the tidal elevations applied along the open boundary located in the Indian Ocean. For this model run, a depth-independent constant value of 0.003 for the bottom drag coefficient was used throughout the domain. When both external and direct gravitational (tidal potential) forcing mechanisms with the bottom friction coefficient of 0.003 were applied, the modelling results, mostly for the semidiurnal tides, differed significantly from the observations. For the principal semidiurnal constituents (M_2, S_2, N_2, K_2), these simulations produced degenerated amphidromic systems with virtual amphidromes located in Saudi Arabia. Contrary to the observations, these results also indicated that the semidiurnal outgoing (reflected) waves were larger than the ingoing waves. When the model was driven by both external and direct forcing a use of either larger constant bottom drag coefficients (0.005 or larger) or depth-dependent bottom friction coefficients (the Manning type friction law with the break depth of 30 m or less as defined in http://adcirc.org/) did not improve modelling results and model-observation comparisons. The bottom friction terms (7) are a sole sink of energy of the barotropic tides in the version of the ADCIRC model used here. Thus, one of the efforts was focused on increasing the energy loss of the outgoing semidiurnal waves by applying the bottom friction coefficient of 0.01 at the

model nodes between the African coast and the major axis of the Red Sea, while 0.003 was used at the remaining grid nodes. This effort also did not generate more realistic results for the semidiurnal tides. At the same time, simulations from the different model setups produced almost identical results for the diurnal tides in the Red Sea.

In summary, the model that produced the results presented here is:

- Depth integrated, two dimensional.
- Driven by Indian Ocean tidal boundary levels; eight tidal constituents.
- Has a much higher resolution than any previous models.
- Was run for a year to give high resolution of tidal frequencies.
- Has a depth-independent friction drag coefficient of 0.003.

Model Validation

There are many ways of comparing the model performance with actual observations. The overall comparison with, for example, the co-tidal chart in Figs. 2.2 and 2.4, is that the essential details are well reproduced. Results also agree generally with the basic mapping of Yang et al. (2013), and Madah et al. (2015).

Before proceeding to detailed descriptions based on the model, it is appropriate to make direct comparisons with the observations of tidal constituents in Tables 2.1 and 2.3. For these comparisons, we look at the O_1 constituent as representative of the diurnal constituents, and the M_2 constituent as representative of the semidiurnal constituents. The K_1 and S_2 constituents are less suitable for comparisons because of the air pressure effects noted above.

The first comparison, shown in Table 2.6a, for O_1, bearing in mind that the older observations in many cases are of limited quality, is of the ratio between the computed and observed constituent amplitudes (Hc/Ho), and the differences between the observed and computed phases (Gc-Go) in the third and second columns from the right. All the phase differences have been adjusted to fall in the range -180^0 to $+180^0$ for easier comparison. The amplitude ratio for O_1 is close to the ideal 1.0 for the southern locations, varies in the central region, and is higher than 3.0 in the northern parts of the Red Sea where the model is giving amplitudes bigger than observed. Note however, that the observed maximum amplitudes are very small except in the south, and are typically only one or two centimetres. The O_1 phases are generally in good agreement between observations and the model computations, with the model phases 15 degrees ahead of the observations, which is equivalent to one hour

Table 2.6 (a) Comparison of observed and modelled amplitudes and phases of the O_1 constituent for heritage data (Table 2.1); (b) comparison of observed and modelled amplitudes and phases of the M_2 constituent for heritage data (Table 2.1)

6a

Location	Latitude (N)	Longitude (E)	O1	Observed	O1	Computed				
			H	G	H	G				
Perim	12.63	43.40	18.0	351	19.1	352		1.06	1	1.1
G89	12.73	43.13	15.0	345	15.6	349		1.04	4	1.2
G109	12.73	43.47	15.0	345	16.5	353		1.10	8	2.7
Assab	13.00	42.73	8.5	344	9	344		1.06	0	0.5
Mocha	13.32	43.23	6.1	352	9.9	354		1.62	2	3.8
G108	13.68	42.18	2.0	335	4	331		2.00	−4	2.0
Hudaida	14.83	40.83	1.0	92	2.2	356		2.20	−96	2.5
Ras Khathib	14.92	42.90	1.0	82	2.1	355		2.10	−87	2.3
Kamaran	15.33	42.60	1.0	140	1.5	1		1.50	−139	2.3
Massawa	15.62	39.47	2.0	184	0.4	212		0.20	28	1.7
Harmil Island	16.48	40.18	1.0	180	0.5	180		0.50	0	0.5
Port Sudan	19.60	37.23	2.0	170	1.6	163		0.80	−7	0.5
Muhammad	20.90	37.17	2.0	175	1.7	163		0.85	−12	0.5
Jeddah	21.52	39.13	1.0	161	1.7	156		1.70	−5	0.7
Rabegh	22.73	38.97	4.0	162	1.9	156		0.48	−6	2.1
Quseir	26.10	34.27	2.0	192	2.3	160		1.15	−32	1.2
Shaker Island	27.45	24.03	1.0	178	2.3	160		2.30	−18	1.4
Ashrafi Islands	27.78	33.72	1.0	153	2.5	165		2.50	12	1.5
Tor	28.23	33.62	2.0	159	3	164		1.50	5	1.0
Ras Ghan'd	28.35	33.12	2.0	157	3.3	171		1.65	14	1.4
Zafarana	29.12	32.67	1.0	199	3.9	172		3.90	−27	3.0
Aqaba	29.52	35.00	1.0	146	2.4	160		2.40	14	1.5
Suez	29.93	32.55	1.3	170	4.1	172		3.15	2	2.8
							Average	1.60	−15	1.7
							StDev	0.89	40	0.9

6b

Location	Latitude (N)	Longitude (E)	O1	Observed	O1	Computed			
			H	G	H	G			
Perim	12.63	43.40	18.0	351	19.1	352	1.06	1	1.1
G89	12.73	43.13	15.0	345	15.6	349	1.04	4	1.2
G109	12.73	43.47	15.0	345	16.5	353	1.10	8	2.7
Assab	13.00	42.73	8.5	344	9	344	1.06	0	0.5
Mocha	13.32	43.23	6.1	352	9.9	354	1.62	2	3.8
G108	13.68	42.18	2.0	335	4	331	2.00	−4	2.0
Hudaida	14.83	40.83	1.0	92	2.2	356	2.20	−96	2.5
Ras Khathib	14.92	42.90	1.0	82	2.1	355	2.10	−87	2.3
Kamaran	15.33	42.60	1.0	140	1.5	1	1.50	−139	2.3
Massawa	15.62	39.47	2.0	184	0.4	212	0.20	28	1.7
Harmil Island	16.48	40.18	1.0	180	0.5	180	0.50	0	0.5
Port Sudan	19.60	37.23	2.0	170	1.6	163	0.80	−7	0.5
Muhammad	20.90	37.17	2.0	175	1.7	163	0.85	−12	0.5

Table 2.6 (continued)

6b

Location	Latitude (N)	Longitude (E)	O1	Observed	O1	Computed			
			H	G	H	G			
Jeddah	21.52	39.13	1.0	161	1.7	156	1.70	−5	0.7
Rabegh	22.73	38.97	4.0	162	1.9	156	0.48	−6	2.1
Quseir	26.10	34.27	2.0	192	2.3	160	1.15	−32	1.2
Shaker Island	27.45	24.03	1.0	178	2.3	160	2.30	−18	1.4
Ashrafi Islands	27.78	33.72	1.0	153	2.5	165	2.50	12	1.5
Tor	28.23	33.62	2.0	159	3	164	1.50	5	1.0
Ras Ghan'd	28.35	33.12	2.0	157	3.3	171	1.65	14	1.4
Zafarana	29.12	32.67	1.0	199	3.9	172	3.90	−27	3.0
Aqaba	29.52	35.00	1.0	146	2.4	160	2.40	14	1.5
Suez	29.93	32.55	1.3	170	4.1	172	3.15	2	2.8
							1.60	−15	1.7
							0.89	40	0.9

for diurnal constituents. The comparisons in Table 2.7a, for O_1 with the much better observational data are encouragingly better, with the average modelled amplitudes 40% higher than observed. The phases are now 4.1 degrees behind the observations, equivalent to only 17 min time difference over the whole Red Sea area.

Turning to the semidiurnal M_2 tide, again the ratio between the computed and observed constituent amplitudes (Hc/Ho), and the differences between the observed and computed phases (Gc-Go) are again in the third and second columns from the right. (Hc/Ho) is 0.93, with modelled results slightly less than the observed. The timings show very good agreement except at Assab and Mocha in the south; overall the modelled timings lag the observations by four minutes (2 degrees for semidiurnal terms) but there is a large scatter with a standard deviation of just over an hour. Here all the phase differences have again been adjusted to fall in the range 0^0 to $+360^0$ for easier comparison. The semidiurnal tides are much larger than the diurnal tides except for the amphidrome region in the central Red Sea. The comparisons in Table 2.7b, with the much better new observational data are better in some critical respects, but because many of the new long-term observations are deliberately in the vicinity of the central amphidrome, where the phases change very rapidly along the coasts, the phase differences are inevitably much more critically dependent on exact model locations so there is more error due to our localised sampling. Overall the model phases lag the new data by 32^0, equivalent to one hour. Note however, that on the Saudi Arabian coast the model amplitude shortfall is generally around 60%, and the phases of the M_2 tide lag observations by close to an hour in a consistent pattern. On the opposite Sudan coast near Port Sudan the lag is about 2.5 h. Small shifts of the modelled amphidrome location can easily account for this. Overall the agreement is very good given the small amplitudes of the tidal waves, and the frictional uncertainties discussed above.

Another test of the model viability, which weights comparison toward areas of bigger tidal amplitude, is the amplitude H of the vector difference between observed and predicted tidal amplitude/phase vectors. This is explained in the polar plot of Fig. 2.9. This parameter is computed by Cartesian algebra, for each location and each constituent, from the following expression (Davies et al. 1997):

$$H = \left[\left(A_{obs} \cos g_{obs} - A_{com} g_{com}\right)^2 + \left(A_{obs} \sin g_{obs} - A_{com} \sin g_{com}\right)^2 \right]^{\frac{1}{2}} \tag{9}$$

A and g are amplitudes and phases, respectively, and suffixes "com" and "obs" denote the computed and observed harmonic constants.

For O_1 Table 2.6a shows an average vector difference of 1.7 ± 0.9 cm with the greatest discrepancies in the far north of the Red Sea. Table 2.7a shows even better agreement with a difference vector of only 0.7 ± 0.4 cm.

For the semidiurnal constituents exemplified by M_2, the amplitudes of the difference vector average 14.5 ± 9.0 cm for the older data in Table 2.6b. However, the agreement is much improved by comparisons with the new reliable data set, with difference vector amplitudes of 6.8 ± 5.0 cm. In part, this improvement is due to the concentration of the new measurements where the M_2 amplitudes are small, but overall the model results prove to be robust when tested against the better, new observations.

Table 2.7 (a) Comparison of observed and modelled amplitudes and phases of the **O₁** constituent for new data (Table 2.2); (b) Comparison of observed and modelled amplitudes and phases of the **M₂** constituent for new data (Table 2.2). Amplitude ratios and phase differences are also tabulated. The vector amplitudes are the differences in vector space as shown in Fig. 2.9

Location	Latitude (N)	Longitude (E)		O1 Observed		O1 Computed				
				H	G	H	G			
Swakin	19.12	37.34		2.1	159	1.5	163	0.73	4	0.6
Port Sudan	19.63	37.22		2.0	159	1.6	163	0.78	4	0.5
Sanganeeb	19.73	37.43		1.6	144	1.6	163	0.96	18	0.5
Arkalai	20.23	37.20		1.8	160	1.6	163	0.89	3	0.2
Al Lith	20.15	40.26		1.8	159	1.5	153	0.81	−6	0.4
KAUST	22.31	39.11		1.6	166	1.9	156	1.16	−10	0.4
Ar Rayis	23.52	38.61		1.5	169	2.0	157	1.31	−12	0.6
Gizan	16.93	42.58		1.7	136	0.5	74	0.28	−62	1.5
Al Qunfuda	19.12	41.07		1.7	131	1.2	149	0.72	17	0.6
Jeddah	21.54	39.15		1.7	154	1.7	156	1.01	2	0.1
Yanbau	24.11	38.07		1.4	158	2.0	157	1.44	−1	0.6
Al Wajh	26.24	36.52		1.1	159	2.2	158	2.04	−1	1.1
Duba	27.33	35.73		1.1	161	2.3	159	2.09	−2	1.2
Magana	28.46	34.77		1.0	169	2.4	157	2.36	−12	1.4
			speed	**13.94**				**28.98**		
Location	Latitude (N)	Longitude (E)	M2 Observed		M2 Computed					
			H	G	H	G				
Swakin	19.12	37.34	1.0	176	0.8	258		0.76	82	1.2
Port Sudan	19.63	37.22	1.7	142	0.5	226		0.31	84	1.7
Sanganeeb	19.73	37.43	1.7	140	0.5	210		0.28	71	1.6
Arkalai	20.23	37.20	2.7	131	0.9	160		0.33	29	2.0
Al Lith	20.15	40.26	2.5	329	3.1	346		1.23	17	1.0
KAUST	22.31	39.11	11.0	115	5.3	116		0.48	1	5.7
Ar Rayis	23.52	38.61	14.6	115	7.2	119		0.49	4	7.5
Gizan	16.93	42.58	32.0	295	22.6	313		0.71	18	12.7
Al Qunfuda	19.12	41.07	8.3	294	11.8	334		1.42	40	7.6
Jeddah	21.54	39.15	7.1	97	3.1	108		0.43	11	4.1
Yanbau	24.11	38.07	16.4	101	8.2	121		0.50	20	9.1
Al Wajh	26.24	36.52	23.3	103	12.6	126		0.54	23	12.7
Duba	27.33	35.73	24.9	103	13.5	127		0.54	24	13.7
Magana	28.46	34.77	27.5	110	14.8	128		0.54	18	14.2
							Average	0.61	32	6.8
							StDev	0.33	28	5.0

The *currents* at the KAUST buoy agree in general with the model, but there are some significant differences. For both observations and currents, the semi-major axes align slightly east of north, consistent with the alignment of the nearest Saudi coastline at this latitude, but several degrees clockwise from the general 23 degree west of north alignment of the Red Sea. Note that the maximum north-going currents in the observations are some 2.5 h ahead of high water levels in the northern Red Sea, consistent with standing Kelvin Wave dynamics.

Figure 2.10 plots the two ellipses for **M₂** currents, showing the observed currents are larger than the modelled currents, but the amplitudes are comparable and small. The modelled current ellipse is almost rectilinear. Note the same vertical (Y, north) scales but very different horizontal (X, east) scales, in Fig. 2.10.
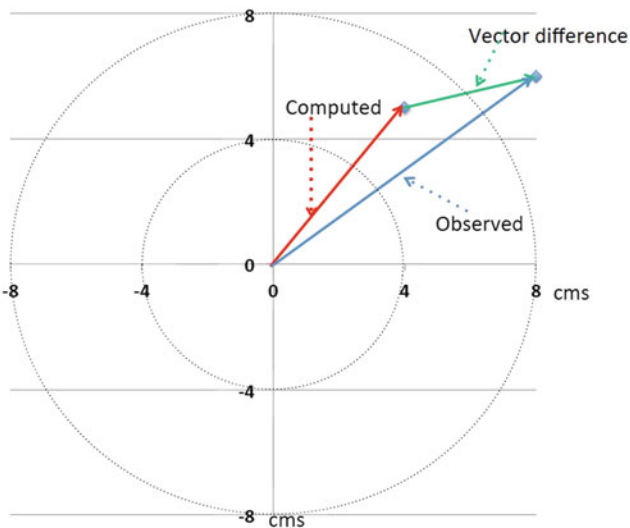
Fig. 2.9 Diagram explaining the difference vector (green) in harmonic constituent comparisons of model (red) and observed (blue) tidal constituent amplitudes and phases plotted in a polar phase coordinate system

In summary, the model agrees well with the better new observations, which means that the modelling of the complexities in the southern Bab el Mandeb Strait entrance are good, as any error there will propagate through the Red Sea. However, there are systematic differences:

- The modelled **diurnal** phases in levels are generally correct to within thirty minutes throughout the Red Sea.
- Diurnal amplitudes are modelled high by about 20% in the central Red Sea, and about 80% high in the north.
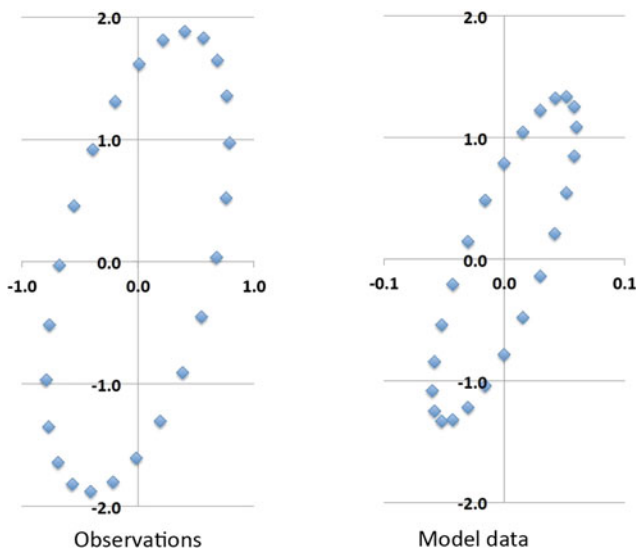
Fig. 2.10 Observed and modelled M_2 current ellipses. Units are cm/s. Note that the vertical (Y) scales are the same, but the X-scale for modelled data is expanded by 10. Y is geographic north positive, and X is geographic east positive. The semi-major axis is 17^0 east of north, while the modelled semi-major axis is 3^0 east of north

- However, diurnal amplitudes are everywhere only about 1.5 cm.
- Semidiurnal amplitudes are around 40 cm at the Bab el Mandeb Strait, then fall to near zero in the central Red Sea, then increase to 30 cm at Suez.
- These **semidiurnal** amplitudes are on average 15% low in the Red Sea but within this average there are clear regional patterns:
    - In the south, model semidiurnal amplitudes are about 200% high.
    - North of the central amphidrome the model results for amplitude are systematically too low, at about 60% of the observed amplitudes.
- Observed currents at the KAUST buoy are larger than the modelled currents and the ellipse is broader.

With these specific comparisons between observations and the model in mind, we can now look at the regional tidal dynamics, as shown by the model, to discuss the Red Sea tides in detail.

Tidal Elevations and Currents

Here we discuss the Red Sea tides, based on the observations and model results.

It is useful to compare the tides inside and outside the Red Sea as separated by the Bab el Mandeb Strait. To define external tides, we have done new detailed analyses. Table 2.8a shows the results of a year of sea level tidal analyses for Djibouti, Aden, and Salalah in Oman, three locations in the Arabian Sea, the first two being approximately 100 and 150 km respectively outside the Bab el Mandeb Strait (see Fig. 2.1a). The analyses, all for the year 2015, are of data extracted from the University of Hawaii Sea Level Center database. There are extensive gaps in the data for Aden and Salalah, but the constituent amplitudes and phases are robust and internally consistent. Using the average values from Table 2.1 as representative of the Red Sea tides the bottom line in Table 2.8a shows that the *age* of the semidiurnal tide, inside and outside the Red Sea, is the same within an hour (20 ± 1). The Form factor (the ratio of the amplitudes $(O_1 + K_1)/(M_2 + S_2)$ which indicates the relative importance of the diurnal to the semidiurnal tides, is 0.83 for Aden and Djibouti, whereas it is 0.39 inside the Red Sea. Outside, the tides are mixed, whereas inside they are dominated by the semidiurnal constituents. This semidiurnal enhancement is due to the effect of semidiurnal resonance in the Red Sea. Although both semidiurnal and diurnal tides are reduced by passage through the southern Bab el Mandeb Strait entrance, the semidiurnal tides are less attenuated due to this compensating internal resonance.

Table 2.8 (a) Comparison of tides in the Gulf of Aden and the Red Sea. Amplitude ratios are normalised to K_1 and M_2; (b) Comparison of Equilibrium Tide and modelled tidal ratios

8a

		Djibouti	Amplitude ratio		Aden	Amplitude ratio		Salalah	Amplitude ratio	Red Sea	
	H	G		H	G		H	G		Table 2.1	
Q1	4.2	354	0.11	4.0	357	0.10	4.6	353	0.13		
O1	19.3	353	0.49	20.0	351	0.52	17.9	348	0.51		
P1	11.9	347	0.30	13.0	1	0.34	10.4	340	0.30		
K1	39.3	350	1.00	38.2	357	1.00	35.1	344	1.00		
N2	13.1	130	0.27	13.3	130	0.27	8.1	134	0.26		
M2	48.2	135	1.00	49.0	136	1.00	30.6	143	1.00		
S2	21.6	155	0.45	21.7	155	0.44	11.8	166	0.39		
K2	6.2	150	0.13	5.9	150	0.12	3.6	170	0.12		
std Obs	49.8			50.7			37.3				
Std residuals	5.3			3.3			6.7				
Hours analysed	8753			4639.0			5958				
Age	20	hours		19	hours		23	hours		19	hours
Type	0.84	mixed		0.82	mixed		1.25	mixed		0.33	semidiurnal

8b

	Red Sea	Arabian Gulf	
		See above	
	Model		Equilibrium tide
Diurnal tides			
Q1	0.11	0.11	0.14
O1	0.51	0.51	0.71
P1	0.32	0.31	0.33
K1	1.00	1.00	1.00
Semidiurnal			
N2	0.27	0.27	0.19
M2	1.00	1.00	1.00
S2	0.44	0.43	0.47
K2	0.10	0.12	0.13

Table 2.8b compares the amplitudes of the major diurnal and semidiurnal constituents in the Red Sea from the model, and outside the Red Sea from the values in Table 2.8a. The agreement between outside and inside ratios (normalised to K_1 and M_2 amplitudes) is good at the 0.01 level, showing the validity of the model's boundary conditions and also of its hydrodynamic processing. The third column in Table 2.8b compares these ratios with those in the direct gravitational global tide, the Equilibrium Tidal forcing. Compared with the Equilibrium Tide, in the Red Sea the Q_1 and O_1 tides are 40 percent weaker relative to K_1; and the semidiurnal N_2 is enhanced by some 50% relative to M_2,

while the S_2 solar semidiurnal term, is just a few percent less.

We now give an overall description of the Red Sea tides based on observations and essentially on the patterns defined by the model outputs. Figures 2.11, 2.12, 2.13 and 2.14 display the tidal charts, the computed co-amplitudes (in cm) and co-phases (in hours, relative to UTC (GMT)) of the tidal elevations for the O_1, K_1, M_2 and S_2 constituents. For very similar charts for additional tidal constituents Q_1, P_1, N_2 and K_2, see Jarosz and Blain (2010).

As discussed above (Table 2.8a), due to semidiurnal resonance, except for the Bab el Mandeb Strait and the
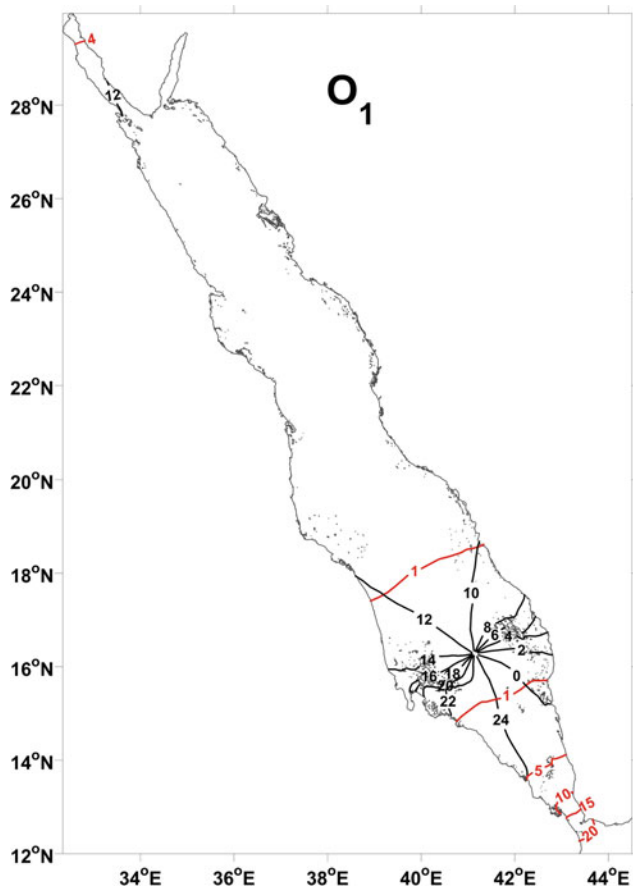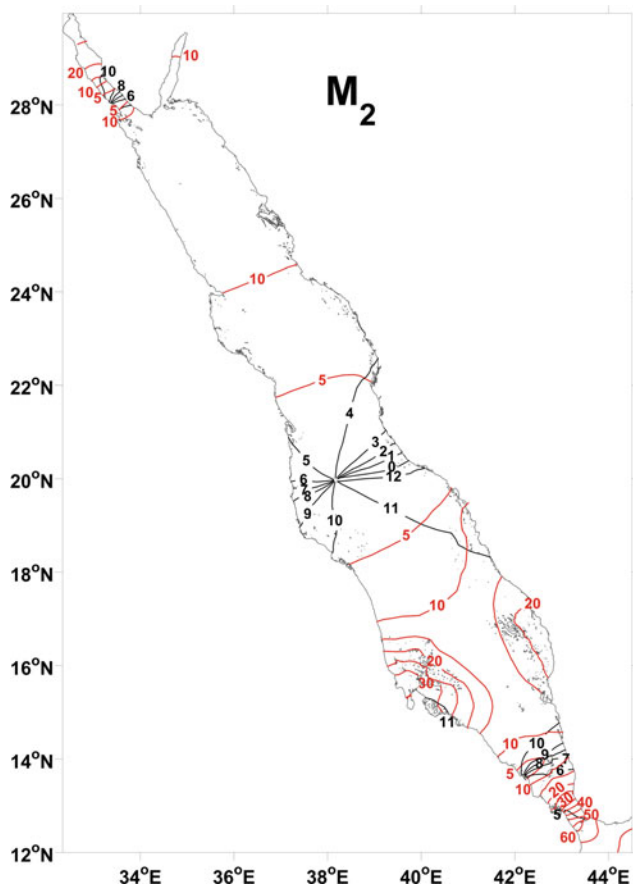
Fig. 2.11 Model coamplitudes (in cm; red lines) and cophases (hours, GMT; black lines) for the **O₁** constituent
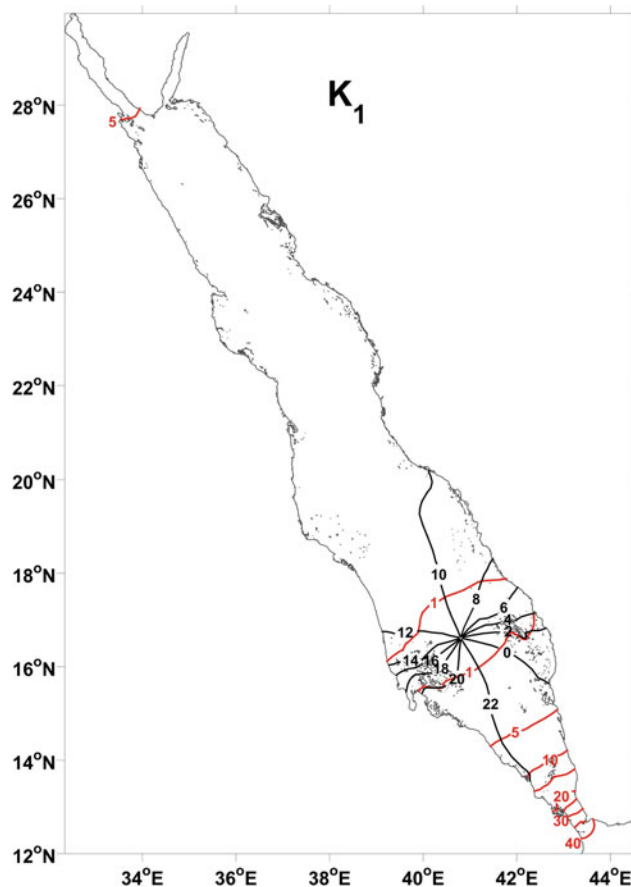
Fig. 2.12 Model coamplitudes (in cm; red lines) and cophases (hours, GMT; black lines) for the **K₁** constituent

central semidiurnal nodal region, the tides in the Red Sea are mainly semidiurnal. The tides in the Bab el Mandeb Strait are mixed, mainly semidiurnal (Jarosz et al. 2005a). The tidal regime is diurnal in the amphidromic systems east of Port Sudan and in the southern Gulf of Suez where the semidiurnal tides are weak in the vicinity of amphidromes.

The amplitudes of the diurnal tidal components (Figs. 2.11 and 2.12) show very similar behaviour in the Red Sea, with little variability in the cross-sea direction. The largest values are found near and in the Bab el Mandeb Strait. In the Red Sea proper, the diurnal amplitudes are less than 5 cm. The major diurnal constituents have well-developed anticlockwise amphidromic systems in the Red Sea (K_1 at approximately $16^0 30'N$; O_1 at approximately 16^0N). The O_1 wavelength is slightly longer than K_1, as the period is longer, so the O_1 amphidrome is displaced farther south from the reflecting node at the north end of the Red Sea.

The amplitudes and phases of the major semidiurnal constituents also have similar distributions to each other. However, they show more complex behaviour than the diurnal constituents (Figs. 2.13 and 2.14). The semidiurnal

amplitudes show large variability in the along-sea direction. They also show some variations in the cross-sea direction between latitudes 15^0N and 17^0N (Dahlak and Farasan Banks). The largest constituent amplitudes are found in the Bab el Mandeb Strait, the Gulf of Suez, and around Dahlak Bank. Moreover, the amplitude and phase distributions indicate that the semidiurnal waves have three amphidrome locations, the main one in the centre between Jeddah and Port Sudan. Only the central amphidrome is fully developed as a counter-clockwise system with an amphidromic point located near 20^0N. The two other areas of Kelvin wave cancelling are examples of degenerate amphidromes: One is located at the northern end of the Bab el Mandeb Strait and another is in the southern part of the Gulf of Suez. Vercelli (1925) and Defant (1961), based on the limited data, postulated the amphidromic point of the M_2 tide in the Bab el Mandeb Strait, located near Assab, southwest of that suggested by the model results. The location of the Suez nodal system is well replicated by the model simulation; it is due to slow wave progression and corresponding short tidal wavelengths, in the relatively shallow waters of the Gulf of Suez.

Fig. 2.13 Model coamplitudes (in cm; red lines) and cophases (hours, GMT; black lines) for the M_2 constituent
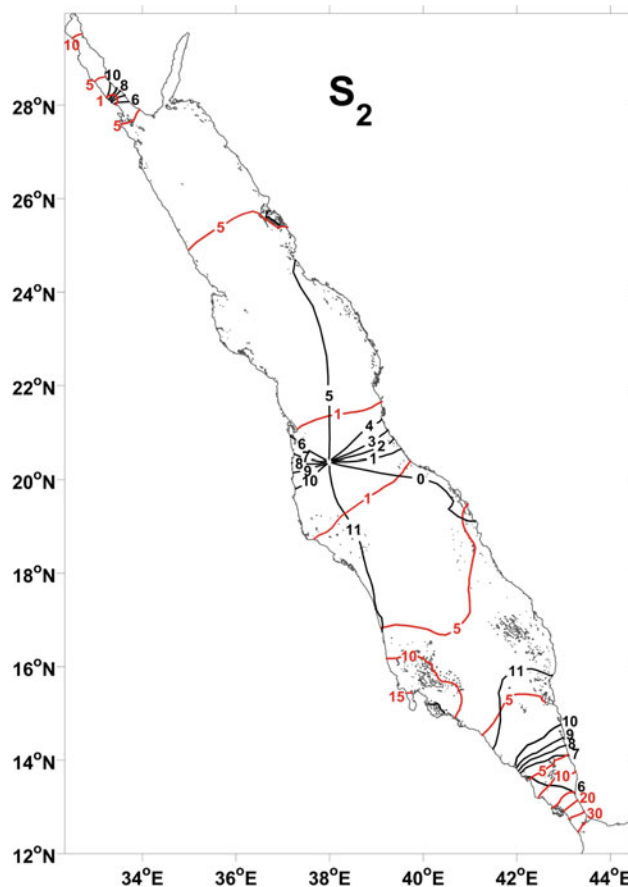

Fig. 2.14 Model coamplitudes (in cm; red lines) and cophases (hours, GMT; black lines) for the S_2 constituent

The model also gives tidal currents. These are generally very weak. The amplitudes and inclination of the semi-major axis for M_2, are shown in Fig. 2.15 (the inclination angles were re-interpolated on a coarser grid for clarity). For all principal tidal components, distributions of the semi-major axis amplitudes show amplification of tidal currents as they flow into the Bab el Mandeb Strait from the Gulf of Aden. The strongest diurnal currents are generated by the K_1 constituent (semi-major axis current amplitudes of the O_1, P_1, and Q_1 are, on average, 47%, 32%, and 9%, respectively, of those associated with K_1) and the M_2 constituent (semi-major axis amplitudes of the S_2, N_2, and K_2 are, on average, 44%, 27%, and 10%, respectively, of those associated with M_2). These current ratios are consistent with the wave amplitude ratios discussed above. Furthermore, the most energetic flow is present in the narrowest southern part of the Bab el Mandeb Strait with the maximum modelled amplitudes found near Perim where, for instance, the speeds of the K_1 and M_2 currents may reach over 40 cm/s.

Farther north, the diurnal currents are below 5 cm/s, except for the K_1 current amplitudes in the southern part of the Gulf of Suez, where they can reach 10 cm/s. The direction of the maximum flow is generally aligned with the major axis of the Sea; however, there is some variability in inclination angles on the shallows, near the islands and coast. Semi-minor axis amplitudes are everywhere much less that the semi-major axis, so diurnal tidal currents are always nearly rectilinear in the Red Sea. In addition, the phase difference between the tidal elevation and maximum tidal velocity is usually approximately 90^0 for all diurnal constituents.

The semi-major axes of the semidiurnal constituent ellipses, as for the diurnal ones, are the largest in the Bab el Mandeb Strait, just north of it, and in the Gulf of Suez; however, their amplitudes are also enhanced on the Farasan and Dahlak Banks and nearby. The direction of the maximum flow is aligned with the along-sea direction, except for regions such as the Farasan and Dahlak Banks (areas of shallow water less than 50 m in depth) where it can be locally quite variable. As for amplitudes, in general, the semidiurnal tidal currents are much stronger in the central and northern Red Sea than those generated by the diurnal tides. Semidiurnal tidal currents are everywhere, except locally near shallow coastal waters, nearly rectilinear, and
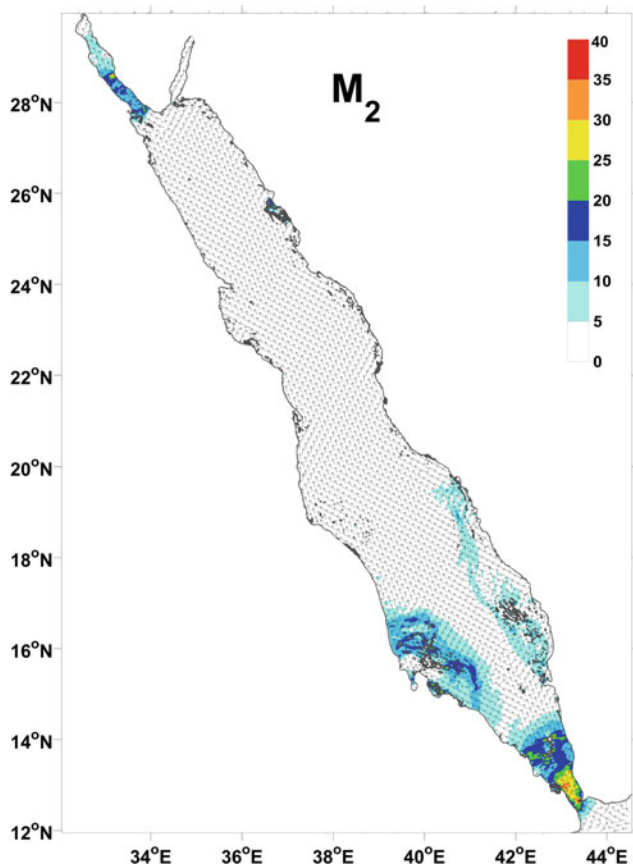
Fig. 2.15 Currents: the major axis (colourbar, in cm/s) and direction of the major axis of the M_2 constituents

typically around 4 cm/s amplitude. The phase distributions for the semidiurnal constituents display more variability in the Red Sea than those of the diurnal tidal currents. Rapid phase changes are found in the southern part of the Sea, near the islands and coast. Additionally, for the N_2 phase the model shows more variability in the deep waters, while the S_2 phase is quite variable in the Gulf of Suez. Moreover, the tidal elevations and the maximum tidal currents for all semidiurnal constituents are such that maximum currents occur at mid-tidal levels, (phase differences of 270^0 or 90^0) as is typical for the dynamics of basin seiche resonances; see Pugh and Woodworth (2014) for further illustrations.

Details of spring-neap modulations in elevations and currents are given in Jarosz and Blain (2010). In general, the tidal residuals are very weak. The highest residual speeds are in the Bab el Mandeb Strait but they do not exceed 0.6 cm/s. The strongest residual flow is generally found in the narrow southern part of the Strait. In the Red Sea, the residual currents are even weaker and do not exceed 0.1 cm/s. Hence,

the residual tidal flow contributes little to the mean circulation observed in the Red Sea, though it may be more important in the Gulf of Suez shallow region.

Locating the Amphidrome

We now consider the observed locations and movement of the central Red Sea semidiurnal amphidrome.

The daily location of the amphidrome can be determined with the help of a numerical model, either continuously, or for an individual tidal constituent. It can also be directly located from the tidal values at the sites surrounding it. This location can be determined for individual tidal constituents, and there is also the possibility of fixing the location on a day-by-day basis (Pugh 1981).

We used the hourly values of sea levels and sub-surface pressures at the three Sudan sites, Akurari, Port Sudan and Swakin, and the two Saudi Arabian sites of Al Lith and KAUST. First, we remove the weather effects by preparing a set of tidal predictions using a full set of constituents for each site. A least-squares **daily** harmonic analysis was then made of 25 hourly values from midnight to midnight to determine the amplitude (H) and phase (G) of the semidiurnal tide, conveniently called D_2, and the diurnal tide, for all five stations. Figure 2.16 shows the semidiurnal D_2 amplitudes. The KAUST amplitudes are significantly greater than the amplitudes at the other four sites, nearer to the amphidrome. There are strong systematic patterns, with spring-neap and other periods, among the tidal syntheses for each station. The G values (not plotted) are related to midnight on each day and so advance on average by 24° per day.

The daily values of H and G at the five stations form a set from which the amphidrome position on each day can be estimated. This was done by fitting least-squares planes to the surfaces Hsin(G) and Hcos(G), which themselves represent the sea levels at a quarter of a tidal period separation. The subsurface pressure values were corrected for the daily air pressure cycle. For each plane, there is a line where it intersects the zero sea level plane, and along which the amplitudes are zero at that time. The second plane, fitted three hours later will have another line of zero sea levels. An intersection of these two lines is the location where there are no semidiurnal sea level changes at any time, and this is the amphidrome location. The amphidrome location changes daily as indicated by the blue diamonds in Fig. 2.17. This distribution also shows a clear pattern, with locations concentrated along line orthogonal to the Red Sea axis. Fitting two planes can be justified by the small (millimetre) values

Fig. 2.16 The D_2 semidiurnal tidal constituent amplitude determined on a daily basis. KAUST is significantly north of the amphidrome. At Swakin the tide is sometimes near zero. Note that all D_2 determinations are independent of eachother, and that the pattern is consistent
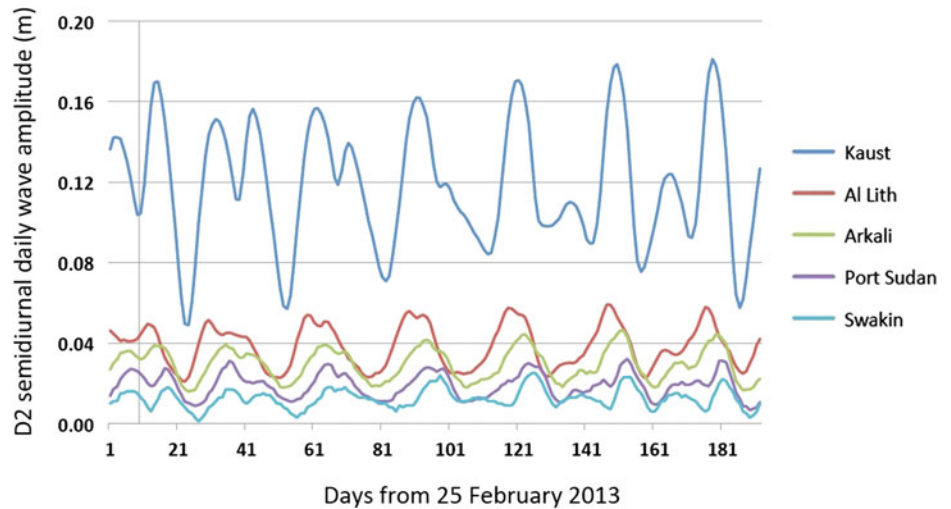
of the residuals; we are dealing with very small tidal amplitudes in this area so millimetre differences are probably in the noise level.

The position of the M_2 amphidrome using all five locations is 38.109^0E, 19.699^0N. Using only three locations, Al Lith, Akurari and Swakin, the position is 38.152^0E, 19.692^0N. The difference is only 5 km. Figure 2.17 also confirms the robustness of the amphidrome positions. M_2 amphidrome positions omitting KAUST, Arkali, Port Sudan and Swakin in turn shows differences of only a few kilometres. However, the inclusion of Al Lith, close to the amphidrome on the Saudi Arabian coast, proved necessary
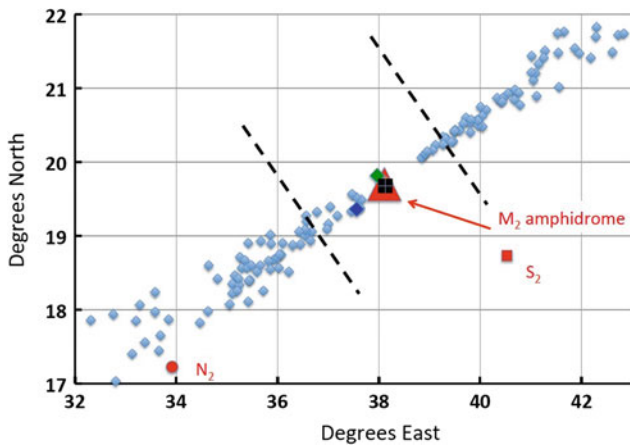
Fig. 2.17 The daily semidiurnal tidal amphidrome positions as a function of latitude and longitude. The M_2 amphidrome position determined over the full six –month period (five stations) is the big red triangle. The black dashed line shows the approximate location of the Sudan and Saudi Arabia coastlines. To test the stability of the solutions, the corresponding positions omitting in turn Arkali (dark blue diamond), Kaust (black square), Swakin (green diamond) and Port Sudan (hidden behing the black square) are shown. Omitting Al Lith produced unstable solutions. The positions for S_2 and N_2 are also shown

for a viable position. The positions of the N_2 and S_2 amphidromes are also plotted; the S_2 is located away from the line of normal daily positions, probably due to the distorting atmospheric pressure effects on the subsurface pressures, but N_2 is displaced as expected for amphidrome movement away from the central axis for bigger tidal amplitudes (N_2 and M_2 combined) (Pugh 1981).

The alignment of the blue diamonds in Fig. 2.17 along a line which is at right angles to the central Red Sea axis confirms the validity of our two-Kelvin-wave model. Figure 2.18 shows the daily positions with the axis rotated 23^0 anticlockwise from north, the best fit to the along-Red Sea axis. The X-axis scale is compressed here, showing that even the more extreme daily positions are close to the theoretical line. The actual position of a central axis for Kelvin wave dynamics is not easily estimated because of coastal curvature and the wide distribution of coral reefs. However, by plotting on a Red Sea Admiralty chart (number 158) the displacement of the amphidrome at 38.109^0E and 19.699^0N from an estimated geographical central axis is between 45 and 60 km. The dashed blue line in Fig. 2.18 covers the estimated position of the central line where the two wave amplitudes would be equal, and the width of the line represents the uncertainty in estimating its position.

We can compare movement with the theoretical expressions in Eqs. 4 and 5. For the northern end of the Red Sea, in the Gulf of Suez, and the S_2/M_2 ratio of 0.25 (Table 2.1), the frequency has maximum and minimum values of 29.29^0/h and 28.18^0/h, above and below the average of 28.98^0/h (see Lamb 1932, Sect. 224; Pugh 1981). If the amphidrome is on average (i.e., for M_2) 800 km from the wave reflection at the northern end of the Red Sea, then at spring tides the amphidrome will move 10 km north, nearer to the reflecting point, and at neap tides the amphidrome will be 6 km farther south, away from the reflecting point.

Fig. 2.18 The amphidrome positions in kilometres, with the Y-coordinate rotated 23^0 anticlockwise from north, along an axis closely aligned to the Red Sea axis. The dashed vertical line is the estimated central axis Y = 0
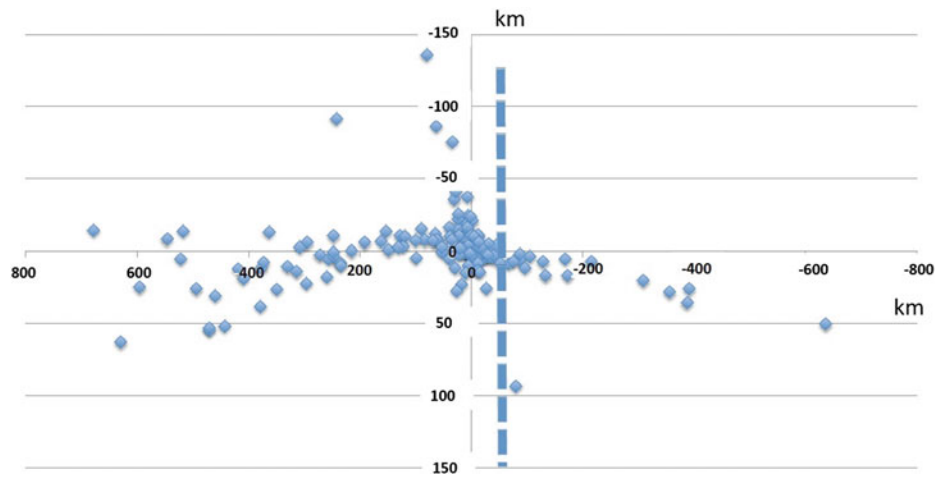
The cross-sea y-axis amphidrome displacements will depend on the relative incident and reflected wave amplitudes, α, or more specifically as the natural logarithm of α, ln α (Eq. 4b). More energy is lost at spring tides than at neaps because of the stronger currents, and so it is expected that the reflected wave will be relatively weaker during spring tides, and that at these times the amphidrome can be displaced farther toward the Sudan coast.

As Eq. (4b) shows, the displacement also depends on the latitude and the water depth. For the Red Sea at 20^0N, the

displacement from the centre is plotted in Fig. 2.19 as a function of α, the incident/reflected Kelvin wave amplitude ratio. The approximate Red Sea coastal boundaries are plotted as vertical dashed red lines. The amphidrome would be degenerate for α values less than 0.85.

Figure 2.20 shows the amphidrome displacement from the northern reflection as a function of the daily semidiurnal tidal range, as represented by the range at KAUST. The coordinates are again as in Fig. 2.2. There is some scatter, but the overall trend is consistent with the movement

Fig. 2.19 The relationship between the amplitude ratio of the ingoing and outgoing waves, and the amphidrome displacement

The dashed lines show the approximate Sudan and Saudi Arabian coasts at 20^0 latitude.

Kilometers displacement from central line
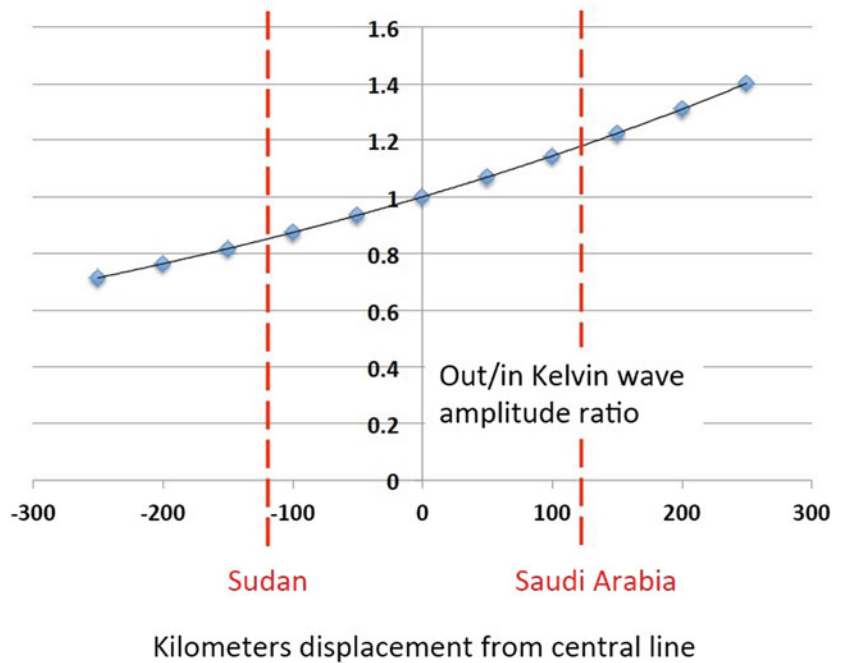
Fig. 2.20 The relationship between daily D_2 semidiurnal amplitudes at KAUST, and the X-displacement of the amphidrome from its mean position, with coordinates aligned along and orthogonal to the Red Sea axis. This is related to the changes of the wave period from spring to neap tides. The red lines show spring and neap ranges at KAUST. The black line is the theoretical displacement from Eq. 4a
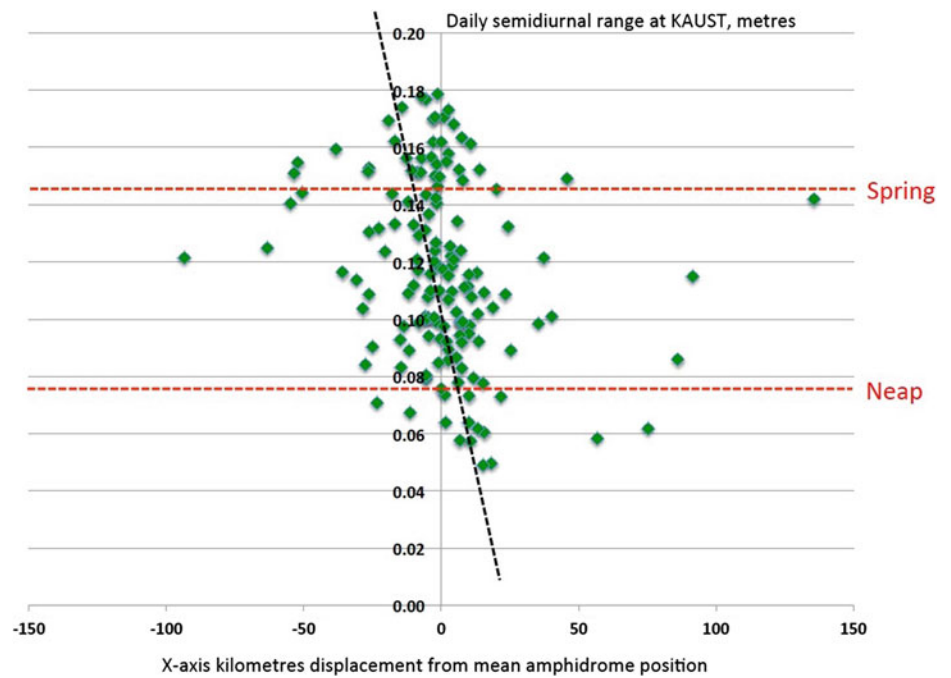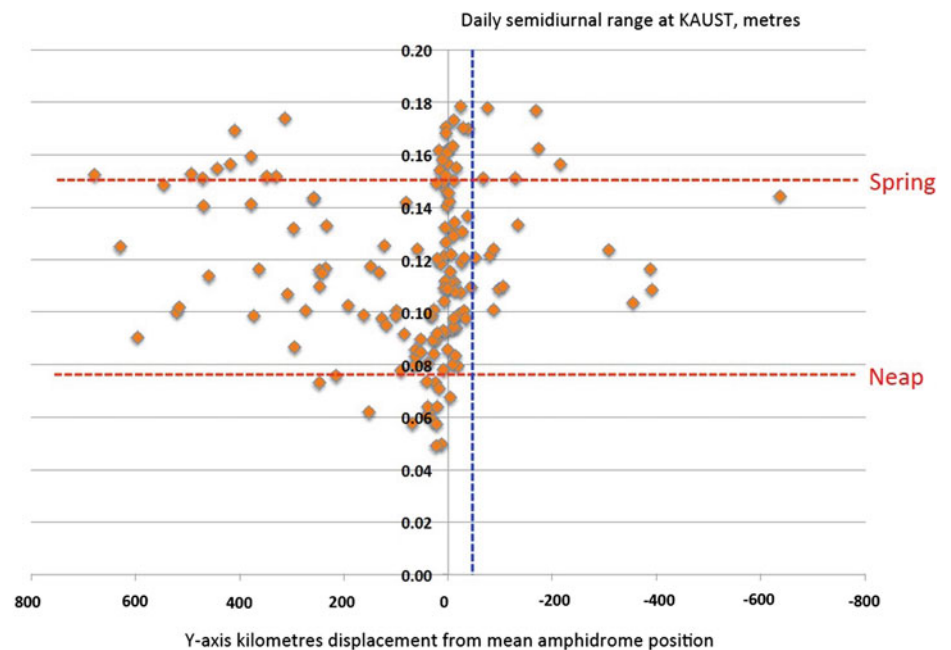
Fig. 2.21 The relationship between daily D_2 semidiurnal amplitudes at KAUST, and the Y-displacement of the amphidrome from its mean position, with coordinates aligned along and orthogonal to the Red Sea axis (Fig. 2.2). This is related to the ratio of incident and reflected Kelvin wave amplitudes

southward at neap tides and northward at springs. The dashed black line shows the theoretical relationship as in Eq. 4a.

Figure 2.21 shows the displacement from the central axis also using the coordinates as in Fig. 2.2. The blue line is the estimated central axis. Almost all values are showing a weaker reflected Kelvin wave, though there are some cases of a larger outgoing wave with positions to the right. The displacements mostly cluster about the mean, with no systematic increase as tidal ranges increase, though it is worth

noting that there is a tendency for the larger displacements to occur on the larger tidal ranges in the upper left quadrant.

Energy Budget

Tidal Energy

It is interesting to estimate tidal energy losses in the Red Sea and to relate them to the total global tidal energy budget.

Table 2.9 Energy fluxes into the Red Sea through the Hanish Sill transect (from Jarosz et al. 2005a, 2005b)

Values are in Gigawatts							
	O1	K1	N2	M2	S2	Spring	Neaps
Flux	0.005	0.018	0.016	0.187	0.016	0.726	0.055
Global dissipation				**2500**			
				0.01	Per cent		

Tidal energy is dissipated by friction in shelf seas, and also by losses to internal tides in the deep ocean Munk (1997). About 1 TW of energy is lost in the deep ocean, generally near areas of rough seabed topography. This energy is thought to be lost through internal tide generation and dissipation, a process which substantially contributes to the energy needed to maintain the large-scale thermohaline circulation of the ocean. Our two-dimensional Red Sea model cannot capture this internal energy sink process.

The dissipation in shallow water due to bottom friction is concentrated in areas of resonance and large tides. The first five areas are: Hudson Bay/Labrador (260 GW), European Shelf (210 GW), Yellow Sea (150 GW), NW Australian Shelf (150 GW) and the Patagonian Shelf (110 GW). Together, they account for more than half the estimated 1.6 TW of M_2 total shelf dissipation. The total diurnal and semidiurnal shallow water dissipation is 2.5 TW. The total dissipation in the deep ocean due to internal tides, and in the shallow water areas due to bottom friction is estimated as 3.5 TW (see Pugh and Woodworth (2014) for a more detailed global discussion).

The dissipation in the Red Sea is very small by comparison, but is worth evaluating as there are many such marginal seas that can contribute to the energy budget. First, we review the two methods available to us for computing energy fluxes and dissipation.

Fluxes Across Boundaries

The tidal energy transmitted across a boundary may be calculated by integrating the energy fluxes that are computed from observed currents and elevations, or currents and elevations computed by numerical models. Clearly, if numerical models represent the currents and elevations over an area correctly, they must include the correct distribution of the areas of frictional energy dissipation.

The instantaneous flux of energy per unit of cross section, in the direction of current U is:

$$Flux = (H + \zeta)\rho\left(\frac{1}{2}|U|^2 + g\zeta\right)U \quad (10a)$$

where ρ is the water density, g is gravitational acceleration, H is the water depth and ζ is the sea level difference from the mean sea level. This expression includes both the kinetic and potential energy fluxes. Fluxes are computed in the X and Y directions for each iteration and averaged over the period of each constituent for O_1, K_1, N_2, M_2 and S_2. The results for the flow across a section at the Hanish Sill are given in Table 2.9.

For a unit width of section over a tidal cycle, the fluxes can also be computed directly from the harmonic constituents:

$$\text{average energy flux} = \frac{1}{2}\rho g D H_0 U_0 \cos\left(g_{\zeta_0} - g_{U_0}\right) \quad (10b)$$

where (H_0, g_{ζ_0}) and (U_0, g_{U_0}) are the amplitudes and phases of the elevations and currents for a particular constituent (see Pugh and Woodworth 2014, Appendix D).

For a progressive wave, the currents and elevations are in phase and the currents are at a maximum at the same time as high water. As a result, there is maximum energy flux in the direction of the wave propagation. For a standing wave, there is no net energy flux because the currents and elevations are 90^0 out of phase, with maximum currents coinciding with the mid-tidal level. In the real world, a perfect standing wave cannot develop because there must be some energy lost at the reflection, and this energy must be supplied by a progressive wave component.

Calculation of the total energy flux due to combinations of all the tidal harmonic constituents is very easy; they may be independently added arithmetically in the same way as the variance at several frequencies in a time series may be added. In general terms, the energy flux is proportional to the square of the constituent amplitudes, so that for the Red Sea the S_2 energy flux is only about 10% of the M_2 flux, and the energy flux due to other constituents is negligible.

Frictional Dissipation

Energy losses in shallow seas result in a systematic adjustment of the tidal patterns and amphidrome locations as described earlier (Pugh 1981).

Frictional energy losses are related to the cube of the current speed, which means that much more energy is absorbed from the Kelvin wave at spring tides than at neap tides. It also means that dissipation is a localised phenomenon, in our case especially at the northern end in the Gulf of Suez. As a result, the reflection coefficient α for the wave is much less at spring tides, and so the amphidrome displacement from the centre is greater. We might expect to see some spring-neap effects in the Y-displacement of the Red Sea central amphidrome, though this is not evident in Fig. 2.21.

Over a spring-neap cycle the average value of dissipation (Jeffreys 1976) is:

$$U_{M_2}^3 \left(1 + \frac{9}{4}\gamma^2 + \frac{9}{64}\gamma^4\right) \qquad (11)$$

where γ is the ratio of the S_2 and the M_2 current constituent amplitudes. For the Equilibrium Tide the ratio $\gamma = 0.46$, which implies that the average energy dissipated over a spring-neap cycle is 1.48 times that dissipated by M_2 alone.

In the northern Red Sea, where $\gamma = 0.3$ (Table 2.3) the average dissipation over a spring-neap cycle is 1.20 times the M_2 dissipation.

Figure 2.22 shows the energy losses in watts per square metre, for spring tides.

Almost all diurnal and semidiurnal tidal energy, which is advected to or/and generated in the Red Sea, is dissipated below 18^0N. There are also enhanced dissipation rates, especially for the energetic semidiurnal constituents, in the Gulf of Suez. Table 2.9 shows the flux into the Red Sea through a transect at the Hanish Sill (Fig. 2.22). The M_2 fluxes are much higher than for any other constituent. Note that representing any internal tidal dissipation is not possible in our two-dimensional model.

On this basis, the tidal energy actually lost in the Red Sea is less than 0.01% of that dissipated globally. Dissipation for M_2 in the Bab el Mandeb Strait entrance may be 0.02% of the global total (Jarosz et al. 2005a).

Internal and External Forcing

Proudman (1953), Defant (1961) and others have reflected on the importance of direct gravitational forcing on Red Sea tides. Although we found the best fit to the observation was obtained when the model was driven only by external Gulf
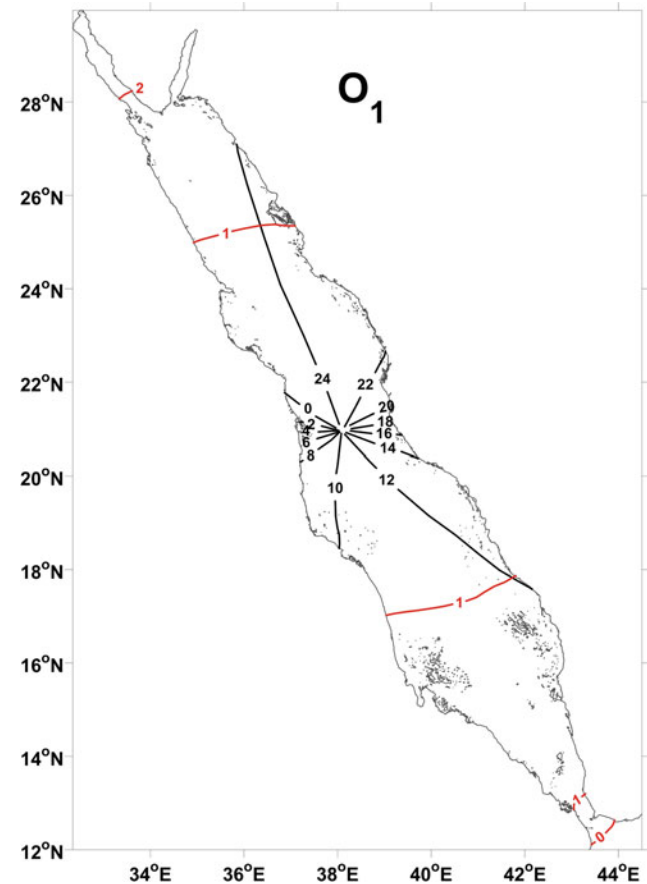

Fig. 2.22 Tidal energy dissipation rate (W/m^2) for spring tides. Also shows the Hanish Sill transect (Table 2.9)

Fig. 2.23 Co-tidal map for the direct forcing only, for O_1

Fig. 2.24 Co-tidal map for the direct forcing only for M_2

The resulting co-tidal maps represent the best published representation of the four principal tidal constituents, O_1, K_1, M_2 and S_2. A caution is necessary when interpreting the K_1 and S_2 maps, because subsurface pressure observations include effects of twelve-hour oscillations of air pressure on tides in the tropics in the atmospheric pressures.

Our best-fit maps using the model are driven by Gulf of Aden forcing only; it was not necessary to include forcing by direct gravitational effects. While a scientifically satisfying model output would include all forcing and fit the observations exactly, this proved impossible despite several experimental model adjustments, mainly by locally adjusting friction coefficients. Possible unmodelled effects may include lateral boundary friction in the extensive shallow coral reefs (we assumed a no-slip boundary condition), and energy losses to coastal lagoons and internal tides. One of the most important omissions may point to the limits of two-dimensional tidal modelling in semi-enclosed seas, because of the loss of energy due to internal tidal dissipation; in general, internal tidal dissipation increases as the square of the amplitudes, whereas frictional barotropic energy losses are related to the cube of the current speed (Green and Nycander 2013). A full three-dimensional model would be needed to include these effects.

The central semidiurnal amphidrome is well reproduced in models, and we have located its position more exactly by using daily tidal analyses from the local coastal stations. The movements of this amphidrome through a spring-neap cycle due to small frequency changes were clearly seen in the daily positions, but orthogonal movement due to varying energy dissipation was less evident.

Future modelling, necessarily three-dimensional, may address and incorporate the impact of direct gravitational forcing, and reduce small but systematic differences for observations. Meanwhile, the results published here represent a major advance on any previously published tidal representations.

of Aden tides, we have also run the model driven only by direct forcing within the Red Sea. The results for both O_1 and M_2 are shown in Figs. 2.23 and 2.24. Tides were allowed to radiate energy out of the Bab el Mandeb Strait. Both charts have distinct amphidromes. The O_1 diurnal tides are quite small, but the M_2 semidiurnal tides have amplitudes of more than 10 cm on the Dahlak Bank.

Conclusions

Although they have small ranges, the tides of the Red Sea have been of considerable historical scientific interest. This is because they can be modelled as classical quarter-(diurnal) and half-(semidiurnal) Kelvin wave resonance. The first numerical model of tides was developed for the Red Sea. However, rigorous testing of the many published model outputs has been limited by the very limited supply of sea level data and tidal analyses for the region.

In this chapter, we have presented important new data from several sources, and tested a hitherto unpublished 2-D hydrodynamic model against the solid observational base.

References

Abohadima S, Rakha KA (2013) Finite element analysis of tidal currents over the Red Sea. Hydrology 1(2):12–17. https://doi.org/10.11648/j.hyd.20130102.11

Blain CA, Rogers WE (1998) Coastal tide prediction using the ADCIRC-2DDI hydrodynamic finite element model: model validation and sensitivity analyses in the southern North Sea/English Channel. Formal Report NRL/FR/ 7322-98-9682, Naval Research Laboratory, Stennis Space Center, MS, 92 pp

Davies AM, Kwong SCM, Flather RA (1997) A three-dimensional model of diurnal and semi diurnal tides on the European shelf. J Geophys Res 102:8625–8656

Defant A (1961) Physical oceanography. Pergamon Press, 598 pp

DHI (1963) Handbuch fur das rote Meer und der Golf von Aden. Deutches Hydrographisches Institute, No. 2034

Egbert GD, Erofeeva SY (2002) Efficient inverse modelling of barotropic ocean tides. J Atmosph Oceanic Technology 19:183–204

Elfatih BAE (2010) Tides analysis in the Red Sea in Port Sudan and Gizan. Thesis, Geophysical Institute, University of Bergen, M.Sc

Foreman MGG (1977) Manual for tidal heights analysis and prediction. Pac Mar Sci Rep 77–10. Institute of Ocean Sciences, Patricia Bay, B.C., Canada, p 101

Foreman MGG (1978) Manual for tidal currents analysis and prediction. Pac Mar Sci Rep 76–6. Institute of Ocean Sciences, Patricia Bay, B.C., Canada, p 70

Gill AE (1982) Atmosphere-ocean dynamics. Academic Press, 662 pp

Grace S (1930) The semi-diurnal tidal motion of the Red Sea. Mon Not Roy Astr Soc Geophys Suppl (March), p 274

Green JAM, Nycander J (2013) A comparison of tidal conversion parameterizations for tidal models. J Phys Oceanography 43:104–119. https://doi.org/10.1175/JPO-D-12-023.1

Harris RA (1898) Manual of Tides. Published in five parts between 1894 and 1907. U.S. Coast and Geodetic Survey Report. Washington. The Red Sea analyses are in Part four. A modern reprint is available

Hendershott MC (1981) Long waves and ocean tides. In: Warren BA, Wunsch C (eds) Evolution of physical oceanography. MIT Press, Cambridge, MA, pp 292–341

International Hydrographic Organization (IHO), Tidal Constituent Bank (1979) Station Catalogue. Ocean and Aquatic Sciences, Dept. of Fisheries and Oceans, Ottawa, Canada

Jarosz E, Blain CA (2010) High resolution model of the barotropic tides for the Red Sea. Final Report to WHOI, February 2010

Jarosz E, Murray SP, Inoue M (2005a) Observations on characteristics of tides in the Bab El Mandeb Strait. J Geophys Res 110:C03015. https://doi.org/10.1029/2004JC002299

Jarosz E, Blain CA, Murray SP, Inoue M (2005b) Barotropic tides in the Bab El Mandeb Strait. Cont Shelf Res 25:1225–1247

Jeffreys H (1976) The Earth, its origin, history and physical constitution (6th Edition). Cambridge University Press, Cambridge, p 574

Kolar RL, Gray WG, Westerink JJ, Luettich RA (1994) Shallow water modeling in spherical coordinates: equation formulation, numerical implementation, and application. J Hydraul Res 32:3–24

Lamb H (1932) Hydrodynamics. Cambridge University Press, 738 pp

Lefevre F, Lyard FH, Le Provost C (2002) FES99: a global tide finite element solution assimilating tide gauge and altimetric information. J Atmos Oceanic Technol 19:1346–1356

Luettich RA, Westerink JJ, Scheffner NW (1992) ADCIRC: an advanced three-dimensional circulation model for shelves, coasts and estuaries, Report 1: Theory and methodology of ADCIRC-2DDI and ADCIRC-3DL. Dredging Research Program Technical Report DRP-92-6, U.S. Army Engineers Waterways Experiment Station, Vicksburg, MS, 137 pp

Lynch DR, Gray WG (1979) A wave equation model for finite element tidal computations. Comp Fluid 7:207–228

Madah F, Mayerle R, Bruss G, Bento J (2015) Characteristics of tides in the Red Sea region, a numerical model study. Open J Marine Sci 5:193–209. https://doi.org/10.4236/ojms.2015.52016

Mohamad KAIA (2012) Sea level variation in the Red Sea based on SODA data. Thesis, Geophysical Institute, University of Bergen, M.Sc

Monismith SG, Genin A (2004) Tides and sea level in the Gulf of Aqaba (Eilat). J Geophys Res 109:C04015

Morcos SA (1970) Physical and chemical oceanography of the Red Sea. Oceanogr Mar Biol Ann Rev 8:73–202

Munk W (1997) Once again: once again—tidal friction. Prog Oceanog 40:7–35

Murray SP, Johns W (1997) Direct observations of seasonal exchange through the Bab el Mandeb Strait. Geophys Res Lett 24:2557–2560

Naval Oceanographic Office (NAVOCEANO) (1997) Data base description for Digital Bathymetric Data Base-Variable Resolution (DBDB-V), Version 1.0. Internal Report, Naval Oceanographic Office, Stennis Space Center, MS

Patzert WC (1974) Wind-induced reversal in Red Sea circulation. Deep Sea Res 21:109–121

Proudman J (1953) Dynamical oceanography. Methuen, London, p 410

Pugh DT (1981) Tidal amphidrome movement and energy dissipation in the Irish Sea. Geophys J R Astron Soc 67:515–527

Pugh DT, Woodworth PL (2014) Sea-level science: understanding tides, surges, tsunamis and mean sea level changes. Cambridge University Press, 395 pp

Pugh DT, Abualnaja Y (2015) Sea-Level changes. In: Rasul NMA, Stewart ICF (eds) the red sea: the formation, morphology, oceanography and environment of a young ocean basin. Springer Earth System Sciences, Berlin Heidelberg, pp 317-328. https://doi.org/10.1007/978-3-662-45201-1_18

Ray RD, Ponte RM (2003) Barometric tides from ECMWF operational analyses. Ann Geophys 21:1897–1910

Reid RO (1990) Water level changes. In: Herbich J (ed) Handbook of coastal and ocean engineering. Gulf Publishing, Houston, TX

Schwiderski EW (1980) On charting global ocean tides. Rev Geophys 18:243–268

Sultan SAR, Ahmad F, Elghribi NM (1995) Sea level variability in the central Red Sea. Oceanol Acta 18(6):607–615

Sultan SAR, Elghribi NM (2003) Sea level changes in the central part of the Red Sea. Indian J Marine Sci 32:114–122

Taylor GI (1920) Tidal friction in the Irish Sea. Phil Trans Roy Soc London A 220:1–33. https://doi.org/10.1098/rsta.1920.0001

Taylor GI (1922) Tidal oscillations in gulfs and rectangular basins. Proc London Math Soc S20:148–181. https://doi.org/10.1112/plms/s2-20.1.148

Vercelli F (1925) Richerche di oceanografia fisica eseguite della R. N. AMMIRAGILIO MAGNAGHI (1923–24), Part I. Correnti e mare. Annali Idrografici 11:1–188

Vercelli F (1927) Richerche di oceanografia fisica eseguite della R. N. AMMIRAGILIO MAGNAGHI (1923–24), Part IV, La temperatura e la salinita. Annali Idrografici 11:1–66

Vercelli F (1931) Nuove ricerche sullen correnti marine nel Mar Rosso. Annali Idrografico 12:424–428

Wahr J (1981) Body tides on an elliptical, rotating, elastic and oceanless Earth. Geophys J R Astron Soc 64:677–703

Westerink JJ, Blain CA, Luettich RA, Scheffner NW (1994) ADCIRC: an advanced three-dimensional circulation model for shelves, coasts and estuaries. Report 2: Users manual for ADCIRC-2DDI.

Dredging Research Program Technical Report DRP-92-6, U.S. Army Engineers Waterways Experiment Station, Vicksburg, MS, 156 pp

Yang Y, Zuo J, Li J, Jia Sun J, Wei Tan W (2013) Simulation of the tide in the Red Sea and the Gulf of Aden. Proceedings of the twenty-third (2013) International offshore and polar engineering anchorage, Alaska, USA, June 30–July 5, 2013. Published by the international society of offshore and polar engineers (ISOPE). ISBN 978-1-880653-99–9; ISSN 1098-6189